Evaluation of the reliability of a heat and mass transfer model in hygroscopic material

Julien Berger, Thomas Busser, Sohail Reddy, George S. Dulikravich

To cite this version:

Julien Berger, Thomas Busser, Sohail Reddy, George S. Dulikravich. Evaluation of the reliability of a heat and mass transfer model in hygroscopic material. International Journal of Heat and Mass Transfer, 2019, 142, pp.118258 -. 10.1016/j.ijheatmasstransfer.2019.06.014 . hal-03487328

HAL Id: hal-03487328
https://hal.science/hal-03487328

Submitted on 20 Dec 2021

Evaluation of the reliability of a heat and mass transfer model in hygroscopic material

Julien Berger [a*], Thomas Busser[b], Sohail Reddy[c], George S. Dulikravich[c]

April 9, 2019

[a] Univ. Grenoble Alpes, Univ. Savoie Mont Blanc, CNRS, LOCIE, 73000 Chambéry, France
[b] Univ. Lyon, ENS de Lyon, Univ Claude Bernard, CNRS, Laboratoire de Physique, 46 Allée d'Italie, 69007 Lyon, France
[c] Department of Mechanical and Materials Engineering, Florida International University, Miami, Florida
*corresponding author, e-mail address : julien.berger@univ-smb.fr

Abstract

The reliability of a model is its accuracy in predicting the physical phenomena. In this paper, the robustness of a model of heat and mass transfer in a porous material is evaluated by comparing the numerical predictions with experimental observations. An experimental facility composed of an enclosure made with spruce CLT panels is used. An increase of temperature is applied in the inside air volume to force the heat transfer from the inner to the outer surfaces. Sensors inside the material enables to have experimental observations of the physical phenomena. Before bench-marking the numerical model, a first set of experimental data is used to reduce the two major source of uncertainties in the model. Indeed, the first source arises from surface heat and mass transfer coefficients, usually determined by empirical correlations. The second comes the thermal conductivity of the material which is defined through standard methods as invariant for the three layers of the spruce panels. To overcome this issue, a set of seven uncertain parameters are estimated using an hybrid optimizer after demonstrating their theoretical and practical identifiability. Then, the reliability of the numerical model, based on the Du Fort–Frankel explicit scheme, is evaluated by comparison to a second set of experimental data obtained in another wall of the enclosure. A very satisfactory agreement is remarked showing the accuracy of the model to predict the physical phenomena in this hygroscopic porous material.

Key words: heat and mass transfer; porous media; bench-marking with experimental data; Du Fort–Frankel scheme; parameter estimation problem

Nomenclature and symbols

Latin letters, physical parameters

c_m	mass storage coefficient	$\left[\mathrm{kg}/\mathrm{m}^3\right]$
$c_{m,0}\,,\,c_{m,1}\,,\,c_{m,2}$	parameter of the mass storage coefficient function	$\left[\mathrm{kg}\cdot\mathrm{Pa}/(\mathrm{m}^3\cdot\mathrm{K})\right]$
c_{mq}	mass storage coefficient due to temperature	$\left[(\mathrm{kg}\cdot\mathrm{Pa})/(\mathrm{m}^3\cdot\mathrm{K})\right]$
$c_q\,,\,c_{q,0}\,,\,c_{q,1}\,,\,c_{q,2}\,,\,c_{q,3}$	heat storage coefficient	$\left[\mathrm{J}/(\mathrm{m}^3\cdot\mathrm{K})\right]$
$c_v\,,\,c_l\,,\,c_a$	specific heat	$\left[\mathrm{J}/(\mathrm{kg}\cdot\mathrm{K})\right]$
h_m	surface mass transfer coefficient	$\left[\mathrm{m}^2/(\mathrm{K}\cdot\mathrm{s})\right]$
h_q	surface heat transfer coefficient	$\left[\mathrm{W}/(\mathrm{m}^2\cdot\mathrm{K})\right]$
$k_m\,,\,k_{m,0}\,,\,k_{m,1}$	mass permeability coefficient	$\left[\mathrm{s}\right]$
k_{mq}	thermo-diffusion coefficient	$\left[\mathrm{kg}/(\mathrm{m}\cdot\mathrm{s}\cdot\mathrm{K})\right]$
$k_q\,,\,k_{q,0,i}\,,\,i\,=\,\left\{1\,,\,2\,,\,3\right\}$	heat transfer coefficient	$\left[\mathrm{W}/(\mathrm{m}\cdot\mathrm{K})\right]$
$k_{q,1}$	parameter of the heat transfer coefficient function	$\left[\mathrm{W}/(\mathrm{m}\cdot\mathrm{K}^2)\right]$
L	length	$\left[\mathrm{m}\right]$
$P_v\,,\,P_{\mathrm{sat}}$	pressure	$\left[\mathrm{Pa}\right]$
R_v	water vapor gas constant	$\left[\mathrm{J}/(\mathrm{kg}\cdot\mathrm{K})\right]$
$r_v\,,\,r_{v,0}$	latent heat of evaporation	$\left[\mathrm{J}/\mathrm{kg}\right]$
T	temperature	$\left[\mathrm{K}\right]$
$t\,,\,t_{\mathrm{f}}\,,\,t_{\mathrm{cpu}}$	time	$\left[\mathrm{s}\right]$
x	space coordinate	$\left[\mathrm{m}\right]$

Latin letters, dimensionless parameters

$F\,,\,F^{u}\,,\,F^{v}$	Fisher information matrix	$\left[-\right]$
J	cost function	$\left[-\right]$
p_k	unknown parameter	$\left[-\right]$
R_{cpu}	computational time ratio	$\left[-\right]$
u	vapor pressure field	$\left[-\right]$
v	temperature field	$\left[-\right]$

Greek letters, physical parameters

ϕ	relative humidity	$\left[\varnothing\right]$
ρ	specific mass	$\left[\mathrm{kg}/\mathrm{m}^3\right]$
ω	mass content	$\left[\mathrm{kg}/\mathrm{m}^3\right]$
δ_x	uncertainty on sensor location	$\left[\mathrm{m}\right]$
$\sigma_{m,P}$	uncertainty on vapor pressure due to sensor measurement	$\left[\mathrm{K}\right]$
$\sigma_{t,P}$	uncertainty on vapor pressure due to sensor time response	$\left[\mathrm{K}\right]$
$\sigma_{x,P}$	uncertainty on vapor pressure due to sensor location	$\left[\mathrm{K}\right]$
$\sigma_{m,T}$	uncertainty on temperature due to sensor measurement	$\left[\mathrm{K}\right]$
$\sigma_{t,T}$	uncertainty on temperature due to sensor time response	$\left[\mathrm{K}\right]$
$\sigma_{x,T}$	uncertainty on temperature due to sensor location	$\left[\mathrm{K}\right]$
$\sigma_{m,\phi}$	uncertainty on relative humidity due to sensor measurement	$\left[-\right]$
Δx	space discretisation parameter	$\left[\mathrm{m}\right]$
Δt	time discretisation parameter	$\left[\mathrm{s}\right]$

Greek letters, dimensionless parameters

γ	coupling parameter of the heat transfer equation	$[-]$
δ	coupling parameter of the mass transfer equation	$[-]$
η	coupling parameter of mass storage due to temperature	$[-]$
Ω_p	set of unknown parameters	$[-]$
Θ	sensitivity coefficient for temperature field	$[-]$
Λ	sensitivity coefficient for vapor pressure field	$[-]$
Ψ, Ψ^u, Ψ^v	determinant of Fisher matrix	$[-]$
σ	variance	$[-]$
ϵ_k	estimator error on the identification of parameter p_k	$[-]$
$\varepsilon_r^{P_v}$	relative error for vapor pressure field	$[-]$
ε_r^T	relative error for temperature field	$[-]$
$\lambda_i, \kappa_i, \theta, \mu_i, \nu_i, i = \{1, 2, 3\}$	numerical model parameters	$[-]$

Dimensionless numbers

Fo^q	Fourier number for heat transfer	$[-]$
Fo^m	Fourier number for mass transfer	$[-]$
Bi	Biot number	$[-]$
Le	Lewis number	$[-]$
$\mathtt{Le}$	modified Lewis number	$[-]$

Subscripts and superscripts

f	final
m	mass transfer
q	heat transfer
mq	coupled mass coefficient under heat process
L	Left boundary $x = 0$
R	Right boundary $x = L$
$\star$	dimensionless parameter
∞	air ambient field
0	initial value at $t = 0$
$\circ$	estimated parameter
apr	*a priori* parameter
num	numerical solution
obs	observation of the field
cpu	computational time

The following symbols are used in the mathematical notation:

- $=$ designates the equality between two scalar numbers. $a = b$ means that the scalars a and b are the same.
- $\overset{\text{def}}{:=}$ stands for a definition. $a \overset{\text{def}}{:=} b$ means that a is defined to be equal to b.
- $\equiv$ names the equivalence between two functions. $f \equiv g$ means that $\forall x_0 \in \Omega_x$, we have $f(x_0) = g(x_0)$, where Ω_x stands for the domain of existence of functions f and g.

1 Introduction

Due to their environmental impacts, building energy efficiency is a crucial challenge for designers and engineers. It requires an accurate prediction of the heat losses through the walls. Moreover, moisture is an important factor since it impacts performance through latent heat exchange. In this context, several models have been proposed in the literature to predict the physical phenomena of heat and mass transfer in porous material. The governing equations of the mathematical model have been proposed in the early work of Luikov [1]. From this mathematical model, numerical models have been proposed to compute the main fields with a recent overview proposed in [2].

An important issue in elaborating model is their reliability to represent accurately and with confidence the physical phenomena. The robustness can be assessed by comparing the numerical predictions to experimental observations. The latter can be obtained by submitting a porous material to forcing conditions at its boundaries. Sensors are settled inside the material to generate local experimental measurements of the fields. On the other hand, the model is defined based on the heat and mass conservation equation combined with boundary conditions. The reliability of the model needs to be checked for Robin-type boundary conditions since there are used in practical applications to represent the physical phenomena at the interface between the material and the ambient air.

In the literature, various work aims at proposing such comparisons. Nevertheless, two important sources of uncertainties can be remarked in the attempt of validating the robustness of the model. First, the modeling at the interface between the porous material and the ambient air is identified as a source of error. More precisely, the values of the surface heat and mass transfer coefficients are always uncertain. In [3] or [4], the reliability is evaluated considering a configuration with Dirichlet boundary conditions to avoid this uncertainty. In [5], the coefficients are settled using the empirical correlation proposed in [6]. In [7, 8], the coefficients are guessed by changing randomly their values. In [9, 10], the so-called Sherwood number is employed to compute the surface coefficients using the Reynolds number. This approach requires costly computational fluid dynamics. In [11, 12], the coefficients are guessed by performing a sensitivity analysis on the prediction of the physical phenomena.

The second source of discrepancies in the model reliability arises from the determination through the standards methods of the so-called material properties. The knowledge of these parameters is crucial since there are involved in the heat and mass transfer processes [13]. The standards methods are based on steady-state measurement and are particularly questionable for hygroscopic materials [14]. Furthermore, there are not appropriate for materials which are intrinsically composed of several layers such as spruce wood panels. Indeed, according to the standard method (ISO 8302), the thermal conductivity of spruce panels is assumed as invariant inside the material.

Thus, the aim of this work is to evaluate the reliability of a model of heat and mass transfer in a hygroscopic material, reducing the uncertainties due to the material properties and to the heat and mass surface transfer coefficients. The measurements are obtained using an experimental set-up composed of enclosures, which panels are based on three spruce layers. The fields of the inside and outside air volumes can be controlled as forcing conditions. Sensors are settled in two different walls to obtained experimental measurements of temperature and vapor pressure. To avoid the mentioned sources of uncertainties, a first set of experimental observations is used to determine the uncertain parameters in the models, namely the heat and mass surface transfer coefficients and the thermal conductivity of the three layers composing the panels. Then, another set of experimental observations is used for comparison with the numerical predictions. The article is organized as follows. Section 2 presents the mathematical model and its dimensionless formulation. Then, in Section 3, the numerical model is detailed. An innovative approach, based on the Du Fort–Frankel numerical scheme, is used to reduce the computational cost of the direct computation. In Section 4, the methodology to solve the parameter estimation problem

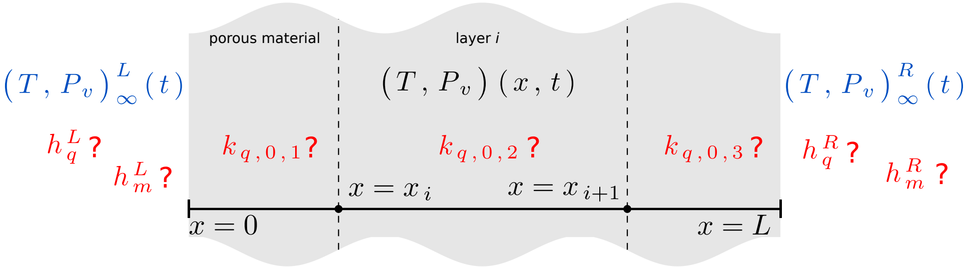

Figure 1. *Illustration of physical problem with the unknown parameters.*

is presented. The experimental facility to generate the observation of temperature and vapor pressure is introduced in Section 5. In Section 6, the identifiability of the unknown parameters is demonstrated. Then, the results of the parameter estimation problem, using the first set of observations, are given. Finally, in Section 7, the reliability of the model is compared to another set of experimental observations.

2 Description of the mathematical model

Fist, the governing equations of the mathematical model are described. An illustration of the problem is given in Figure 1. A porous material is submitted to forcing conditions of temperature and vapor pressure on each boundary. The transfer occurs in a plan perpendicular to the gravity so the effects of the latter are negligible. A total of seven parameters are unknown in the mathematical problem, including the boundary heat and mass surface transfer coefficients and the thermal conductivity of each of the three layers.

2.1 Porous media

The mathematical model describes the heat and mass transfer in multi-layered wall composed of porous media. The transfer are assumed as 1-dimensional and the spatial domain is defined as $x \in \bigl[\,0\,,\,L\,\bigr]$, where $L\;\bigl[\,\mathrm{m}\,\bigr]$ is the thickness of the wall. The physical phenomena are observed for the time $t \in \bigl[\,0\,,\,t_{\,\mathrm{f}}\,\bigr]$. The field of interests are the temperature $T\;\bigl[\,\mathrm{K}\,\bigr]$ and the vapor pressure $P_v\;\bigl[\,\mathrm{Pa}\,\bigr]$ defined according to:

$$\begin{aligned} T \,:\, \Bigl[\,0\,,\,L\,\Bigr] \times \Bigl[\,0\,,\,t_{\,\mathrm{f}}\,\Bigr] &\longrightarrow \mathbb{R}_{>0}\,, & P_v \,:\, \Bigl[\,0\,,\,L\,\Bigr] \times \Bigl[\,0\,,\,t_{\,\mathrm{f}}\,\Bigr] &\longrightarrow \mathbb{R}_{>0}\,, \\ (\,x\,,\,t\,) &\longmapsto T\,(\,x\,,\,t\,)\,, & (\,x\,,\,t\,) &\longmapsto P_v\,(\,x\,,\,t\,)\,. \end{aligned}$$

The saturation pressure $P_{\,\mathrm{sat}}\;\bigl[\,\mathrm{Pa}\,\bigr]$ is given by a temperature dependent function given by the Antoine's law:

$$P_{\,\mathrm{sat}}(\,T\,) \stackrel{\mathrm{def}}{:=} P^{\,\circ}_{\,\mathrm{sat}} \cdot \left(\frac{T \;-\; T_{\,a}}{T_{\,b}}\right)^{\alpha}\,, \qquad\qquad T \geqslant T_{\,a}\,,$$

with $P^{\,\circ}_{\,\mathrm{sat}} \;=\; 997.3\ \mathrm{Pa}\,,\; T_{\,a} \;=\; 159.5\ \mathrm{K}\,,\; T_{\,b} \;=\; 120.6\ \mathrm{K}$ and $\alpha \;=\; 8.275\,$. The moisture content in the porous material is denoted as $\omega\;\bigl[\,\mathrm{kg/m^{\,3}}\,\bigr]$ and the relative humidity by $\phi\;\bigl[\,\varnothing\,\bigr]\,$.

2.2 Governing equation

According to [1], the governing equations of heat and mass transfer in porous media are:

$$\frac{\partial \omega}{\partial t} = \frac{\partial}{\partial x} \cdot \left(k_m \cdot \frac{\partial P_v}{\partial x} \right) + \frac{\partial}{\partial x} \cdot \left(k_{mq} \cdot \frac{\partial T}{\partial x} \right),$$

$$c_q \cdot \frac{\partial T}{\partial t} = \frac{\partial}{\partial x} \cdot \left(k_q \cdot \frac{\partial T}{\partial x} \right) + r_v \cdot \frac{\partial}{\partial x} \cdot \left(k_m \cdot \frac{\partial P_v}{\partial x} \right).$$

The chosen potential to write the governing equations is the vapor pressure. Thus, one can write:

$$\partial \omega = \frac{\partial \omega}{\partial \phi} \cdot \partial \phi + \frac{\partial \omega}{\partial T} \cdot \partial T .$$

It is assumed negligible the variation of the moisture content with temperature $\dfrac{\partial \omega}{\partial T} = 0$. In addition, using the relation between relative humidity and vapor pressure, $\phi = \dfrac{P_v}{P_{\text{sat}}}$, we have:

$$\partial \phi = \frac{1}{P_{\text{sat}}} \cdot \partial P_v - \frac{P_v}{P_{\text{sat}}^2} \cdot \frac{\partial P_{\text{sat}}}{\partial T} \cdot \partial T .$$

The Clapeyron relation gives:

$$\frac{\partial P_{\text{sat}}}{\partial T} = \frac{r_v}{R_v \cdot T^2} \cdot P_{\text{sat}} ,$$

where r_v $[\text{J/kg}]$ is the latent heat of vaporization and R_v $[\text{J/(kg}\cdot\text{K)}]$ the gas constant of water vapor. Using these results, the time variation of moisture content is given by:

$$\frac{\partial \omega}{\partial t} = c_m \cdot \frac{\partial P_v}{\partial t} - c_{mq} \cdot \frac{\partial T}{\partial t} ,$$

where

$$c_m \overset{\text{def}}{:=} \frac{\partial \omega}{\partial \phi} \cdot \frac{1}{P_{\text{sat}}} , \qquad c_{mq} \overset{\text{def}}{:=} c_m \cdot P_v \cdot \frac{r_v}{R_v \cdot T^2} .$$

Thus, the heat and mass transfer is given by the following system of coupled partial differential equations:

$$c_m \cdot \frac{\partial P_v}{\partial t} = \frac{\partial}{\partial x}\left(k_m \cdot \frac{\partial P_v}{\partial x} \right) + \frac{\partial}{\partial x}\left(k_{mq} \cdot \frac{\partial T}{\partial x} \right) + c_{mq} \cdot \frac{\partial T}{\partial t} , \tag{1a}$$

$$c_q \cdot \frac{\partial T}{\partial t} = \frac{\partial}{\partial x}\left(k_q \cdot \frac{\partial T}{\partial x} \right) + r_v \cdot \frac{\partial}{\partial x}\left(k_m \cdot \frac{\partial P_v}{\partial x} \right). \tag{1b}$$

2.3 Material properties

The wall is composed of several layers of wood spruce panels. It is assumed that only the thermal conductivity varies according to each layer. So, other properties do not vary according to the different layers. The sorption curve of the material is given as a third order polynomials. Thus, the storage coefficients are computed using the following functions:

$$c_m(T, P_v) \overset{\text{def}}{:=} \frac{1}{P_{\text{sat}}(T)} \cdot \left(c_{m,0} + c_{m,1} \cdot \frac{P_v}{P_{\text{sat}}(T)} + c_{m,2} \cdot \left(\frac{P_v}{P_{\text{sat}}(T)} \right)^2 \right), \tag{2a}$$

$$c_q(T, P_v) \overset{\text{def}}{:=} c_{q,0} + c_{q,1} \cdot \frac{P_v}{P_{\text{sat}}(T)} + c_{q,2} \cdot \left(\frac{P_v}{P_{\text{sat}}(T)} \right)^2 + c_{q,3} \cdot \left(\frac{P_v}{P_{\text{sat}}(T)} \right)^3 , \tag{2b}$$

$$c_{mq}(T, P_v) \overset{\text{def}}{:=} c_m(T, P_v) \cdot P_v \cdot \frac{r_v(T)}{R_v \cdot T^2} . \tag{2c}$$

The gas constant for water vapor is $R_v = 462 \text{ J/(kg} \cdot \text{K)}$. The thermo-diffusion coefficient k_{mq} $\left[\text{kg/(m} \cdot \text{s} \cdot \text{K)}\right]$ is set as constant. The mass permeability coefficient varies according to temperature and vapor pressure:

$$k_m(T, P_v) \overset{\text{def}}{:=} k_{m,0} + k_{m,1} \cdot \frac{P_v}{P_{\text{sat}}(T)}. \tag{3a}$$

It is assumes that the thermal conductivity varies according to temperature and space:

$$k_q(x, T) \overset{\text{def}}{:=} \sum_{i=1}^{3} k_{q,i}(x, T), \tag{4a}$$

where

$$k_{q,i}(x, T) \overset{\text{def}}{:=} \psi_i(x) \cdot k_{q,0,i} + k_{q,1} \cdot T.$$

The piece-wise function for each layer ψ_i is defined by:

$$\psi_i(x) \overset{\text{def}}{:=} \begin{cases} 1, & x_{i-1} \leqslant x \leqslant x_i, \\ 0, & \text{otherwise}, \end{cases}$$

where x_{i-1} denotes the interface location in the space domain between the layer $i-1$ and i. The three unknown parameters of the material properties are the thermal conductivity coefficients $k_{q,0,i}$ $\left[\text{W/(m} \cdot \text{K)}\right], i = \{1, 2, 3\}$.

The mass transfer under temperature gradient coefficient k_{mq} is set as constant and independent of the fields. The latent heat of vaporization r_v $\left[\text{J/kg}\right]$ depends on temperature according to:

$$r_v(T) \overset{\text{def}}{:=} r_{v,0} + \Big(c_v - c_l\Big) \cdot \Big(T - T_c\Big),$$

with c_v $\left[\text{J/(kg} \cdot \text{K)}\right]$ and c_l $\left[\text{J/(kg} \cdot \text{K)}\right]$ the specific heat of vapor and liquid water, respectively. The numerical values for the physical constants are $r_{v,0} = 2.5 \cdot 10^6 \text{ J/kg}$, $c_v = 1870 \text{ J/(kg} \cdot \text{K)}$, $c_l = 4180 \text{ J/(kg} \cdot \text{K)}$ and $T_c = 273.15 \text{ K}$.

2.4 Initial and boundary conditions

At the initial state, the temperature and vapor pressure are known in the material:

$$T = T^0(x), \qquad P_v = P_v^0(x), \qquad t = 0,$$

where T_0 and $P_{v,0}$ are given function of space:

At the interface between the material and the ambient air, Robin type boundary conditions are assumed for the heat flow

$$k_q \cdot \frac{\partial T}{\partial x} + r_v \cdot k_m \cdot \frac{\partial P_v}{\partial x} = h_q^L \cdot \Big(T - T_\infty^L(t)\Big) + r_v \cdot h_m^L \cdot \Big(P_v - P_{v,\infty}^L(t)\Big), \quad x = 0,$$

$$k_q \cdot \frac{\partial T}{\partial x} + r_v \cdot k_m \cdot \frac{\partial P_v}{\partial x} = -h_q^R \cdot \Big(T - T_\infty^R(t)\Big) - r_v \cdot h_m^R \cdot \Big(P_v - P_{v,\infty}^R(t)\Big), \quad x = L,$$

and for the mass one

$$k_m \cdot \frac{\partial P_v}{\partial x} + k_{mq} \cdot \frac{\partial T}{\partial x} = h_m^L \cdot \Big(P_v - P_{v,\infty}^L(t)\Big), \qquad x = 0,$$

$$k_m \cdot \frac{\partial P_v}{\partial x} + k_{mq} \cdot \frac{\partial T}{\partial x} = -h_m^R \cdot \Big(P_v - P_{v,\infty}^R(t)\Big), \qquad x = L,$$

where the air ambient temperature $T_{\infty}^{L,R}$ and vapor pressure $P_{v,\infty}^{L,R}$ are given time dependent functions. The parameters h_q $\bigl[\mathrm{W/(m^2 \cdot K)}\bigr]$ and h_m $\bigl[\mathrm{m^2/(K \cdot s)}\bigr]$ are the heat and mass surface transfer coefficients. They are the additional four unknown parameters for the left and right boundaries. A relation is introduced between both coefficients using the Lewis Le $[\varnothing]$ number:

$$h_m^L = \frac{h_q^L}{R_v \cdot \rho_a \cdot c_a \cdot \mathrm{Le}^L}\,, \qquad h_m^R = \frac{h_q^R}{R_v \cdot \rho_a \cdot c_a \cdot \mathrm{Le}^R}\,,$$

where $\rho_a = 1.16\ \mathrm{kg/m^3}$ is the dry air specific mass and $c_a = 10^3\ \mathrm{J/(kg \cdot K)}$ the specific heat of dry air.

2.5 Dimensionless formulation

To carry on the numerical analysis, the physical problem is transformed into a dimensionless formulation. For this, the time and space domains are scaled according to:

$$x^\star = \frac{x}{L}\,, \qquad t^\star = \frac{t}{t^{\,\mathrm{ref}}}\,.$$

The fields are also transformed into:

$$u = \frac{P_v}{P_v^{\,\mathrm{ref}}}\,, \qquad v = \frac{T}{T^{\,\mathrm{ref}}}\,.$$

It is important to note that $T^{\,\mathrm{ref}}$ $[\,^\circ\mathrm{C}\,]$ and $P_v^{\,\mathrm{ref}}$ $[\,\mathrm{Pa}\,]$ should not be taken to zero.

The storage and diffusion coefficients as well as the latent heat of vaporization are converted in dimensionless ones:

$$c_m^\star = \frac{c_m}{c_m^{\,\mathrm{ref}}}\,, \qquad c_q^\star = \frac{c_q}{c_q^{\,\mathrm{ref}}}\,, \qquad c_{mq}^\star = \frac{c_{mq}}{c_{mq}^{\,\mathrm{ref}}}\,,$$

$$k_m^\star = \frac{k_m}{k_m^{\,\mathrm{ref}}}\,, \qquad k_q^\star = \frac{k_q}{k_q^{\,\mathrm{ref}}}\,, \qquad k_{qm}^\star = \frac{k_{qm}}{k_{qm}^{\,\mathrm{ref}}}\,, \qquad r^\star = \frac{r_v}{r_{v,0}}\,.$$

In this way, the dimensionless Fourier numbers are defined:

$$\mathrm{Fo}^m = \frac{k_m^{\,\mathrm{ref}} \cdot t^{\,\mathrm{ref}}}{c_m^{\,\mathrm{ref}} \cdot L^2}\,, \qquad \mathrm{Fo}^q = \frac{k_q^{\,\mathrm{ref}} \cdot t^{\,\mathrm{ref}}}{c_q^{\,\mathrm{ref}} \cdot L^2}\,.$$

The coupling parameters between both heat and mass transfer are set:

$$\gamma = \frac{k_m^{\,\mathrm{ref}} \cdot P_v^{\,\mathrm{ref}} \cdot r_{v,0}}{k_q^{\,\mathrm{ref}} \cdot T^{\,\mathrm{ref}}}\,, \qquad \delta = \frac{k_{mq}^{\,\mathrm{ref}} \cdot T^{\,\mathrm{ref}}}{k_m^{\,\mathrm{ref}} \cdot P_v^{\,\mathrm{ref}}}\,, \qquad \eta = \frac{c_{mq}^{\,\mathrm{ref}} \cdot T^{\,\mathrm{ref}}}{c_q^{\,\mathrm{ref}} \cdot P_v^{\,\mathrm{ref}}}\,.$$

For the boundary conditions, the time dependent Biot number is introduced:

$$\mathrm{Bi} = \frac{h_q \cdot L}{k_q^{\,\mathrm{ref}}}\,,$$

as well as a modified Lewis number:

$$\mathtt{Le} = R_1 \cdot \rho_a \cdot c_a \cdot \frac{k_m^{\,\mathrm{ref}} \cdot T^{\,\mathrm{ref}}}{k_q^{\,\mathrm{ref}}} \cdot \bigl(\mathrm{Le}\bigr)^{2/3}\,.$$

In the end, the dimensionless formulation of the heat and mass problem is:

$$c_m^\star \cdot \frac{\partial u}{\partial t^\star} = \mathrm{Fo}^m \cdot \frac{\partial}{\partial x^\star}\left(k_m^\star \cdot \frac{\partial u}{\partial x^\star}\right) + \delta \cdot \mathrm{Fo}^m \cdot \frac{\partial^2 v}{\partial x^{\star\,2}} + \eta \cdot c_{mq}^\star \cdot \frac{\partial v}{\partial t^\star}\,, \tag{5a}$$

$$c_q^\star \cdot \frac{\partial v}{\partial t^\star} = \mathrm{Fo}^q \cdot \frac{\partial}{\partial x^\star}\left(k_q^\star \cdot \frac{\partial v}{\partial x^\star}\right) + \gamma \cdot \mathrm{Fo}^q \cdot r^\star \cdot \frac{\partial}{\partial x^\star}\left(k_m^\star \cdot \frac{\partial u}{\partial x^\star}\right). \tag{5b}$$

The boundary condition becomes for the mass transfer:

$$k_m^\star \cdot \frac{\partial u}{\partial x^\star} + \delta \cdot \frac{\partial v}{\partial x^\star} = \frac{\mathrm{Bi}^L}{\mathtt{Le}^L} \cdot \Bigl(u - u_\infty^L \Bigr), \qquad x^\star = 0, \tag{6a}$$

$$k_m^\star \cdot \frac{\partial u}{\partial x^\star} + \delta \cdot \frac{\partial v}{\partial x^\star} = -\frac{\mathrm{Bi}^R}{\mathtt{Le}^R} \cdot \Bigl(u - u_\infty^R \Bigr), \qquad x^\star = 1, \tag{6b}$$

and for the heat one:

$$k_q^\star \cdot \frac{\partial v}{\partial x^\star} + r^\star \cdot \gamma \cdot k_m^\star \cdot \frac{\partial u}{\partial x^\star} = \mathrm{Bi}^L \cdot \Bigl(v - v_\infty^L \Bigr) + r^\star \cdot \gamma \cdot \frac{\mathrm{Bi}^L}{\mathtt{Le}^L} \cdot \Bigl(u - u_\infty^L \Bigr), \qquad x^\star = 0, \tag{7a}$$

$$k_q^\star \cdot \frac{\partial v}{\partial x^\star} + r^\star \cdot \gamma \cdot k_m^\star \cdot \frac{\partial u}{\partial x^\star} = -\mathrm{Bi}^R \cdot \Bigl(v - v_\infty^R \Bigr) - r^\star \cdot \gamma \cdot \frac{\mathrm{Bi}^R}{\mathtt{Le}^R} \cdot \Bigl(u - u_\infty^R \Bigr), \quad x^\star = 1. \tag{7b}$$

In the dimensionless representation, the unknown parameters are Bi^L, $\mathtt{Le}^L$, Bi^R, $\mathtt{Le}^R$ and $k_{q,0,i}^\star, i = \{1, 2, 3\}$.

3 Direct numerical model

The numerical model used to solve the so-called direct problem is now described. It requires to be efficient by saving computational efforts and providing accurate solutions of the governing equations. These needs are particularly justified in the framework of parameter estimation problem where the direct problem is solved many time.

3.1 The Du Fort–Frankel numerical method

A uniform discretisation is considered for space and time lines. The discretisation parameters are denoted using Δt for the time and Δx for the space. The discrete values of functions $u(x, t)$ and $v(x, t)$ are written as $u_j^n \overset{\text{def}}{:=} u(x_j, t^n)$ and $v_j^n \overset{\text{def}}{:=} v(x_j, t^n)$ with $j = 1, \ldots, N_x$ and $n = 1, \ldots, N_t$. It is remarked that $j = 1$ and $j = N_x$ corresponds to $x = 0$ and $x = 1$, respectively. For the sake of clarity, the super-script * is removed in this section for the description of the numerical method.

The Du Fort–Frankel scheme is employed to build an efficient numerical model for the heat and mass balance equations (5a) and (5b). The original work may be consulted in [15]. It affords an explicit numerical scheme. Thus, no costly sub-iterations are required to treat the nonlinearities, as in implicit approaches. Furthermore, as demonstrated in [16, 17], it has an extended stability region, so the so-called Courant-Friedrichs-Lewy (CFL) condition [18] is not an impediment. Interested readers may consult [16, 17] for further details and its applications for heat and moisture transfer in building porous materials. Since many details are provided in [17] for a similar system of coupled partial differential equations, the demonstration of the fully discrete equations is not detailed.

From Eq. (5a), using the Du Fort–Frankel numerical scheme, the following fully discrete dynamical system is obtained:

$$\begin{aligned} u_j^{n+1} - \frac{1}{1 + \lambda_3} \cdot \Biggl(& \lambda_1 \cdot u_{j+1}^n + \lambda_2 \cdot u_{j-1}^n + \Bigl(1 - \lambda_3 \Bigr) \cdot u_j^{n-1} \\ & + \kappa_1 \cdot v_{j+1}^n + \kappa_2 \cdot v_{j-1}^n - \kappa_3 \cdot \frac{1}{2} \cdot \Bigl(v_j^{n+1} + v_j^{n-1} \Bigr) \\ & + \theta \cdot \frac{v_j^{n+1} - v_j^{n-1}}{2 \cdot \Delta t} \Biggr) = 0, \end{aligned} \tag{8}$$

where the coefficients $\{\,\lambda_i\,\}_{i\,=\,1}^{3}$, $\{\,\kappa_i\,\}_{i\,=\,1}^{3}$ and θ are defined as:

$$\lambda_1 \overset{\mathrm{def}}{:=} 2\cdot\mathrm{Fo}^{\,m}\cdot\frac{\Delta t}{\Delta x^2}\cdot\frac{k^{\,n}_{\,m\,,\,j\,+\,\frac{1}{2}}}{c^{\,n}_{\,m\,,\,j}}\,, \qquad \lambda_2 \overset{\mathrm{def}}{:=} 2\cdot\mathrm{Fo}^{\,m}\cdot\frac{\Delta t}{\Delta x^2}\cdot\frac{k^{\,n}_{\,m\,,\,j\,-\,\frac{1}{2}}}{c^{\,n}_{\,m\,,\,j}}\,, \quad \lambda_3 \overset{\mathrm{def}}{:=} \frac{1}{2}\cdot\Bigl(\lambda_1\,+\,\lambda_2\Bigr)\,,$$

$$\kappa_1 \,=\, \kappa_2 \overset{\mathrm{def}}{:=} 2\cdot\mathrm{Fo}^{\,m}\cdot\frac{\Delta t}{\Delta x^2}\cdot\frac{\delta}{c^{\,n}_{\,m\,,\,j}}\,, \quad \kappa_3 \overset{\mathrm{def}}{:=} \kappa_1\,+\,\kappa_2 \qquad\qquad \theta \overset{\mathrm{def}}{:=} \eta\cdot 2\cdot\Delta t\cdot\frac{c_{\,mq\,,\,j}}{c_{\,q\,,\,j}}$$

Similarly, using the Du Fort–Frankel numerical scheme for Eq. (5b), the fully discrete dynamical system is:

$$\begin{aligned} v_{\,j}^{\,n+1} \,-\, \frac{1}{1\,+\,\mu_3}\cdot\Biggl(&\mu_1\cdot v^{\,n}_{\,j+1} \,+\, \mu_2\cdot v^{\,n}_{\,j-1} \,+\, \Bigl(1\,-\,\mu_3\Bigr)\cdot v_{\,j}^{\,n-1} \\ &+\,\nu_1\cdot u^{\,n}_{\,j+1}\,+\,\nu_2\cdot u^{\,n}_{\,j-1}\,-\,\nu_3\cdot\frac{1}{2}\cdot\Bigl(u_{\,j}^{\,n+1}\,+\,u_{\,j}^{\,n-1}\Bigr)\Biggr) \,=\, 0\,, \end{aligned} \tag{9}$$

with the following coefficients:

$$\mu_1 \overset{\mathrm{def}}{:=} 2\cdot\mathrm{Fo}^{\,q}\cdot\frac{\Delta t}{\Delta x^2}\cdot\frac{k^{\,n}_{\,q\,,\,j\,+\,\frac{1}{2}}}{c^{\,n}_{\,q\,,\,j}}\,, \qquad \mu_2 \overset{\mathrm{def}}{:=} 2\cdot\mathrm{Fo}^{\,q}\cdot\frac{\Delta t}{\Delta x^2}\cdot\frac{k^{\,n}_{\,q\,,\,j\,-\,\frac{1}{2}}}{c^{\,n}_{\,q\,,\,j}}\,,$$

$$\mu_3 \overset{\mathrm{def}}{:=} \frac{1}{2}\cdot\Bigl(\mu_1\,+\,\mu_2\Bigr)\,, \qquad \nu_1 \overset{\mathrm{def}}{:=} 2\cdot\gamma\cdot r^{\,n}_{\,j}\cdot\mathrm{Fo}^{\,q}\cdot\frac{\Delta t}{\Delta x^2}\cdot\frac{k^{\,n}_{\,m\,,\,j\,+\,\frac{1}{2}}}{c^{\,n}_{\,q\,,\,j}}\,,$$

$$\nu_2 \overset{\mathrm{def}}{:=} 2\cdot\gamma\cdot r^{\,n}_{\,j}\cdot\mathrm{Fo}^{\,q}\cdot\frac{\Delta t}{\Delta x^2}\cdot\frac{k^{\,n}_{\,m\,,\,j\,-\,\frac{1}{2}}}{c^{\,n}_{\,q\,,\,j}}\,, \qquad \nu_3 \overset{\mathrm{def}}{:=} \nu_1\,+\,\nu_2\,.$$

Then, the two systems Eqs. (8) and (9), are solved to obtain an explicit formulation of the fields $u_{\,j}^{\,n+1}$ and $v_{\,j}^{\,n+1}$. For the sake of notation compactness, the results are provided in the supplementary `Maple`™ file.

The storage and latent heat of vaporization coefficients are evaluated using the following interpolation:

$$c_{\,j} \overset{\mathrm{def}}{:=} c\,(\,u_{\,j}\,,\,v_{\,j}\,)\,, \qquad\qquad r_{\,j} \overset{\mathrm{def}}{:=} r\,(\,v_{\,j}\,)\,.$$

The diffusion coefficients are interpolated according to:

$$k_{\,j\,+\,\frac{1}{2}} \overset{\mathrm{def}}{:=} k\left(\frac{1}{2}\cdot\Bigl(u_{\,j}\,+\,u_{\,j+1}\Bigr)\,,\,\frac{1}{2}\cdot\Bigl(v_{\,j}\,+\,v_{\,j+1}\Bigr)\right).$$

For the boundary conditions, a second order accurate discretisation in space is used to maintain the accuracy properties. For the boundary $x\,=\,0$, the discretisation of Eqs. (6a) and (7a) yields :

$$\frac{k_{\,m\,,\,1}}{2\cdot\Delta x}\cdot\Bigl(-\,u_3\,+\,4\cdot u_2\,-\,3\cdot u_1\Bigr)\,+\,\frac{\delta}{2\cdot\Delta x}\cdot\Bigl(-\,v_3\,+\,4\cdot v_2\,-\,3\cdot v_1\Bigr) \tag{10a}$$

$$=\,\frac{\mathrm{Bi}^{\,L}}{\mathsf{Le}^{\,L}}\cdot\Bigl(u_1\,-\,u_\infty^{\,L}\Bigr)\,, \tag{10b}$$

$$\frac{k_{\,q\,,\,1}}{2\cdot\Delta x}\cdot\Bigl(-\,v_3\,+\,4\cdot v_2\,-\,3\cdot v_1\Bigr)\,+\,\frac{\gamma\cdot r_1\cdot k_{\,m\,,\,1}}{2\cdot\Delta x}\cdot\Bigl(-\,u_3\,+\,4\cdot u_2\,-\,3\cdot u_1\Bigr) \tag{10c}$$

$$=\,\mathrm{Bi}^{\,L}\cdot\Bigl(v_1\,-\,v_\infty\Bigr)\,+\,\gamma\cdot r_1\cdot\frac{\mathrm{Bi}^{\,L}}{\mathsf{Le}^{\,L}}\cdot\Bigl(u_1\,-\,u_\infty^{\,L}\Bigr)\,. \tag{10d}$$

Then, the system (10) is solved to give an explicit expression of u_1 and v_1. A very similar operation is achieved for the boundary $x\,=\,1$.

3.2 Metrics of efficiency and reliability of a model

To evaluate the efficiency of a numerical model, one criteria is the computational (CPU) run time required to compute the solution. It is measured using the `Matlab`$^{\text{TM}}$ environment with a computer equipped with `Intel` i7 CPU and 32 GB of RAM. The following ratio is defined:

$$R_{\,\mathrm{cpu}} \overset{\mathrm{def}}{:=} \frac{t_{\,\mathrm{cpu}}}{t_{\,\mathrm{f}}}\,,$$

where $t_{\,\mathrm{cpu}}\,[\,\mathrm{s}\,]$ is the measured CPU time and $t_{\,\mathrm{f}}$ is the final physical time of the simulation.

The reliability of a model is assessed by comparing the numerical results with experimental observations. The relative error for temperature or vapor pressure is computed according to:

$$\varepsilon_{\,r}^{\,P_v}\,(\,x_0^{\,\star}\,,t^{\,\star}\,) \overset{\mathrm{def}}{:=} \frac{u^{\,\mathrm{num}}\,(\,x_0^{\,\star}\,,t^{\,\star}\,) \;-\; u^{\,\mathrm{obs}}\,(\,x_0^{\,\star}\,,t^{\,\star}\,)}{u^{\,\mathrm{obs}}\,(\,x_0^{\,\star}\,,t^{\,\star}\,)}\,,$$

$$\varepsilon_{\,r}^{\,T}\,(\,x_0^{\,\star}\,,t^{\,\star}\,) \overset{\mathrm{def}}{:=} \frac{v^{\,\mathrm{num}}\,(\,x_0^{\,\star}\,,t^{\,\star}\,) \;-\; v^{\,\mathrm{obs}}\,(\,x_0^{\,\star}\,,t^{\,\star}\,)}{v^{\,\mathrm{obs}}\,(\,x_0^{\,\star}\,,t^{\,\star}\,)}\,,$$

where $x_0^{\,\star}$ is the sensor location, the super script $^{\mathrm{num.}}$ defined the output field computed with the model and $^{\mathrm{obs.}}$ stands for the experimental observation of the field.

4 Parameter estimation

The purpose is to use experimental observations to retrieve the seven unknown parameters $h_{\,q}^{\,L}\,,\,h_{\,m}^{\,L}\,,\,h_{\,q}^{\,R}\,,\,h_{\,m}^{\,R}\,,\,k_{\,q\,,0\,,1}\,,\,k_{\,q\,,0\,,2}$ and $k_{\,q\,,0\,,3}\,$. Thus, the set of unknown dimensionless parameters is defined by:

$$\Omega_{\,p} \;=\; \big\{\,\mathrm{Bi}^{\,L}\,,\,\mathrm{Bi}^{\,R}\,,\,\mathsf{Le}^{\,L}\,,\,\mathsf{Le}^{\,R}\,,\,k_{\,q\,,0\,,1}^{\,\star}\,,\,k_{\,q\,,0\,,2}^{\,\star}\,,\,k_{\,q\,,0\,,3}^{\,\star}\,\big\}\,.$$

We denote by $p_{\,k}\,$, with $k \;\in\; \big\{\,1\,,\,\ldots\,,\,N_{\,p}\,\big\}$, a component of the set $\Omega_{\,p}\,$. In our case, the total number of unknown parameters is $N_{\,p} \;=\; 7\,$. The distinction is realized between *a priori* parameters $p_{\,k}^{\,\mathrm{apr}}$, used as initial guesses in the optimization procedure and in the computation of the sensitivity equations. The estimated parameter after the optimization process are denoted by $p_{\,k}^{\,\circ}\,$. It is assumed that measurement errors are additive with zero mean, constant variance, uncorrelated and normal distribution.

4.1 Sensitivity equations

To discuss the identifiability of the unknown parameters, the scaled dimensionless local sensitivity functions are introduced for both fields u and v [19, 20]:

$$\Theta_{\,k}\;:\;(\,x\,,\,t\,)\;\longmapsto\;\frac{\sigma_{\,p}}{\sigma_{\,u}}\cdot\frac{\partial u}{\partial p_{\,k}}\,,\qquad \Lambda_{\,k}\;:\;(\,x\,,\,t\,)\;\longmapsto\;\frac{\sigma_{\,p}}{\sigma_{\,v}}\cdot\frac{\partial v}{\partial p_{\,k}}\,,$$

where $\sigma_{\,u}$ and $\sigma_{\,v}$ are the variance of the error measuring u and $v\,$, respectively. The parameter $\sigma_{\,p}$ is set to unity since we assume that prior information on the unknown parameter $p_{\,k}$ has low accuracy and is equal for all parameters. The sensitivity functions are computed by differentiating the governing equations (5a) and (5b) with respect to the unknown parameter $p_{\,k}\,$. The sensitivity equations can be written in a succinct way as:

$$\begin{aligned}
c_m^{\star} \cdot \frac{\partial \Theta_k}{\partial t^{\star}} \;=\; & \mathrm{Fo}^{m} \cdot \frac{\partial}{\partial x^{\star}} \left(k_m^{\star} \cdot \frac{\partial \Theta_k}{\partial x^{\star}} \;+\; \frac{\partial k_m^{\star}}{\partial p_k} \cdot \frac{\partial u}{\partial x^{\star}} \right) \;+\; \delta \cdot \mathrm{Fo}^{m} \cdot \frac{\partial^2 \Lambda_k}{\partial x^{\star\,2}} \\
& +\; \eta \cdot \left(c_{mq}^{\star} \cdot \frac{\partial \Lambda_k}{\partial t^{\star}} \;+\; \frac{\partial c_{mq}^{\star}}{\partial p_k} \cdot \frac{\partial \Lambda_k}{\partial t^{\star}} \right) \;-\; \frac{\partial c_m^{\star}}{\partial p_k} \cdot \frac{\partial u}{\partial t^{\star}}\,, \\
c_q^{\star} \cdot \frac{\partial \Lambda_k}{\partial t^{\star}} \;=\; & \mathrm{Fo}^{q} \cdot \frac{\partial}{\partial x^{\star}} \left(k_q^{\star} \cdot \frac{\partial \Lambda_k}{\partial x^{\star}} \;+\; \frac{\partial k_q^{\star}}{\partial p_k} \cdot \frac{\partial v}{\partial x^{\star}} \right) \;+\; \gamma \cdot \mathrm{Fo}^{q} \cdot \left(\frac{\partial r^{\star}}{\partial p_k} \cdot \frac{\partial}{\partial x^{\star}} \left(k_m^{\star} \cdot \frac{\partial u}{\partial x^{\star}} \right) \right. \\
& \left. +\; r^{\star} \cdot \frac{\partial}{\partial x^{\star}} \left(k_m^{\star} \cdot \frac{\partial \Theta_k}{\partial x^{\star}} \;+\; \frac{\partial k_m^{\star}}{\partial p_k} \cdot \frac{\partial u}{\partial x^{\star}} \right) \right) \;-\; \frac{\partial c_q^{\star}}{\partial p_k} \cdot \frac{\partial v}{\partial t^{\star}}\,.
\end{aligned}$$

The boundary conditions of the sensitivity equations are obtained using a similar approach:

$$\begin{aligned}
& k_m^{\star} \cdot \frac{\partial \Theta_k}{\partial x^{\star}} \;+\; \delta \cdot \frac{\partial \Lambda_k}{\partial x^{\star}} \;=\; \frac{\partial}{\partial p_k} \left(\frac{\mathrm{Bi}^{L}}{\mathsf{Le}^{L}} \right) \cdot \left(u \;-\; u_{\infty}^{L} \right) \;+\; \frac{\mathrm{Bi}^{L}}{\mathsf{Le}^{L}} \cdot \Theta_k \;-\; \frac{\partial k_m^{\star}}{\partial p_k} \cdot \frac{\partial u}{\partial x^{\star}}\,, \qquad x^{\star} \;=\; 0 \\
& k_m^{\star} \cdot \frac{\partial \Theta_k}{\partial x^{\star}} \;+\; \delta \cdot \frac{\partial \Lambda_k}{\partial x^{\star}} \;=\; -\,\frac{\partial}{\partial p_k} \left(\frac{\mathrm{Bi}^{R}}{\mathsf{Le}^{R}} \right) \cdot \left(u \;-\; u_{\infty}^{R} \right) \;-\; \frac{\mathrm{Bi}^{R}}{\mathsf{Le}^{R}} \cdot \Theta_k \;-\; \frac{\partial k_m^{\star}}{\partial p_k} \cdot \frac{\partial u}{\partial x^{\star}}\,, \quad x^{\star} \;=\; 1
\end{aligned}$$

and

$$\begin{aligned}
k_q^{\star} \cdot \frac{\partial \Lambda_k}{\partial x^{\star}} \;+\; r^{\star} \cdot \gamma \cdot k_m^{\star} \cdot \frac{\partial \Theta_k}{\partial x^{\star}} \;=\; & \frac{\partial \mathrm{Bi}^{L}}{\partial p_k} \cdot \left(v \;-\; v_{\infty}^{L} \right) \;+\; \mathrm{Bi}^{L} \cdot \Lambda_k \;+\; \gamma \cdot \frac{\partial}{\partial p_k} \left(r^{\star} \cdot \frac{\mathrm{Bi}^{L}}{\mathsf{Le}^{L}} \right) \cdot \left(u \;-\; u_{\infty}^{L} \right) \\
& +\; r^{\star} \cdot \gamma \cdot \frac{\mathrm{Bi}^{L}}{\mathsf{Le}^{L}} \cdot \Theta_k \;-\; \frac{\partial k_q^{\star}}{\partial p_k} \cdot \frac{\partial v}{\partial x^{\star}} \;-\; \gamma \cdot \frac{\partial}{\partial p_k} \left(r^{\star} \cdot k_m^{\star} \right) \cdot \frac{\partial u}{\partial x^{\star}}\,, \qquad x^{\star} \;=\; 0\,, \\
k_q^{\star} \cdot \frac{\partial \Lambda_k}{\partial x^{\star}} \;+\; r^{\star} \cdot \gamma \cdot k_m^{\star} \cdot \frac{\partial \Theta_k}{\partial x^{\star}} \;=\; & -\,\frac{\partial \mathrm{Bi}^{R}}{\partial p_k} \cdot \left(v \;-\; v_{\infty}^{R} \right) \;-\; \mathrm{Bi}^{R} \cdot \Lambda_k \;-\; \gamma \cdot \frac{\partial}{\partial p_k} \left(r^{\star} \cdot \frac{\mathrm{Bi}^{R}}{\mathsf{Le}^{R}} \right) \cdot \left(u \;-\; u_{\infty}^{R} \right) \\
& -\; r^{\star} \cdot \gamma \cdot \frac{\mathrm{Bi}^{R}}{\mathsf{Le}^{R}} \cdot \Theta_k \;-\; \frac{\partial k_q^{\star}}{\partial p_k} \cdot \frac{\partial v}{\partial x^{\star}} \;-\; \gamma \cdot \frac{\partial}{\partial p_k} \left(r^{\star} \cdot k_m^{\star} \right) \cdot \frac{\partial u}{\partial x^{\star}}\,, \qquad x^{\star} \;=\; 1\,.
\end{aligned}$$

The sensitivity functions qualify the sensitivity of the field according to changes in the parameter p_k. Thus, a small magnitude of the sensitivity function signifies that large changes in p_k induce small changes in the field. Moreover, an optimal evaluation of the unknown parameters is obtained when the sensitivity functions are linearly independent with large magnitudes for all parameters. These information are gathered in the scaled Fisher information matrix [21–23]:

$$F^{u} \stackrel{\mathrm{def}}{:=} \left[F_{ij}^{u} \right], \qquad F^{v} \stackrel{\mathrm{def}}{:=} \left[F_{ij}^{v} \right], \qquad F \stackrel{\mathrm{def}}{:=} \left[F_{ij} \right], \qquad (i, j) \in \{ 1, \ldots, N_p \},$$

where each element of the matrices is computed by:

$$\begin{aligned}
F_{ij}^{u} & \stackrel{\mathrm{def}}{:=} \sum_{q=1}^{N_m} \frac{1}{t_{\mathrm{f}}} \cdot \int_0^{t_{\mathrm{f}}} \Theta_i^{\star}(x_q, t) \cdot \Theta_j^{\star}(x_k, t)\, \mathrm{d}t\,, \\
F_{ij}^{v} & \stackrel{\mathrm{def}}{:=} \sum_{q=1}^{N_m} \frac{1}{t_{\mathrm{f}}} \cdot \int_0^{t_{\mathrm{f}}} \Lambda_i^{\star}(x_q, t) \cdot \Lambda_j^{\star}(x_k, t)\, \mathrm{d}t\,, \\
F_{ij} & \stackrel{\mathrm{def}}{:=} F_{ij}^{u} \;+\; F_{ij}^{v}\,,
\end{aligned}$$

where N_m is the number of observations obtained during the experiments. Moreover, the quality of the experimental design to retrieve the unknown parameters with accuracy is analyzed through the D-optimum criteria:

$$\Psi^{u} \stackrel{\mathrm{def}}{:=} \det F^{u}\,, \qquad \Psi^{v} \stackrel{\mathrm{def}}{:=} \det F^{v}\,, \qquad \Psi \stackrel{\mathrm{def}}{:=} \det F\,.$$

To ensure the maximal accuracy in the estimation of the unknown parameters, it is expected to maximize the quality index Ψ relatively to the measurement plan. Last, an important result is given in [21] using the Cramer–Rao inequality under the assumption stated. An error estimator of the retrieved parameter can be computed according to:

$$\epsilon_k \overset{\text{def}}{:=} \sqrt{\left(F^{-1}\right)_{kk}}\,.$$

High values of ϵ_k might be due to important error during the parameter estimation process.

4.2 Solving the parameter estimation problem

The inverse problem aims at determining the estimated parameter p° verifying:

$$p^{\circ} \overset{\text{def}}{:=} \arg \min_{\Omega_p} J\,, \tag{11}$$

where J is the so-called cost function defined by the least square estimator:

$$J(u, u_{\text{obs}}, v, v_{\text{obs}}) \overset{\text{def}}{:=} w_u \cdot \left|\left| \frac{u - u_{\text{obs}}}{u_{\text{obs}}} \right|\right|_2 + w_v \cdot \left|\left| \frac{v - v_{\text{obs}}}{v_{\text{obs}}} \right|\right|_2\,, \tag{12}$$

where $\left|\left| \bullet \right|\right|_2$ is the $\mathcal{L}_2$ error:

$$\left|\left| \bullet \right|\right|_2 : y \longmapsto \int_0^{t_{\text{f}}} \Big(y(t)\Big)^2 \,\mathrm{d}t\,.$$

The parameters w_u and w_v are weights defined as the variance of the vapor pressure and temperature measurements, respectively. There are essential to scale the cost function J to avoid advantaging one measurement compared to the other [24]. The experimental observations are denoted by u_{obs} and v_{obs}. It also important to mention that the domain of the observations and the solutions of the direct problem verifies dom $u_{\text{obs}} \equiv$ dom u and dom $v_{\text{obs}} \equiv$ dom v.

To solve the parameter estimation problem, an robust technique is used based on the Single-Objective Hybrid Optimizer (SOHO) [25, 26]. It is composed on three individual algorithms, namely the NSGA-III [27], NSDE [28] and MOEA-DD [29]. This combination enables to increase the robustness of the optimization algorithms for a large set of problems. The hybrid optimizer is initialized using one of the three previously mentioned algorithms. The algorithm runs until no longer decreasing in the residual is observed. Then, an alternative algorithm is chosen randomly among the remaining two. By this random selection, the process is made as stochastic to search the optimum parameters and to avoid user bias.

5 Description of the experimental facility

5.1 Set-up

The experimental facility, entirely described in [30], is used to generate the experimental observations. The set-up is an enclosure with an interior volume measuring $0.8 \times 0.88 \times 0.88 = 0.62\,\mathrm{m}^3$, built with 6-cm-thick highly hygroscopic walls composed of CLT panels. A picture of the set-up is shown in Figure 3(a) and one of a slice of CLT panel in Figure 3(b). The latter clearly highlights the three layers of the material. Each layer has a thickness of 2 cm. The cube is placed in a climatic chamber to control the outdoor temperature and relative humidity. The indoor temperature of the enclosure is controlled using four heating resistances connected to a controller. An ultrasonic humidifier, placed outside the facility, injecting droplets of water trough a flexible hose thermally insulated with a silicone rubber sheathing enables to control the relative humidity level.

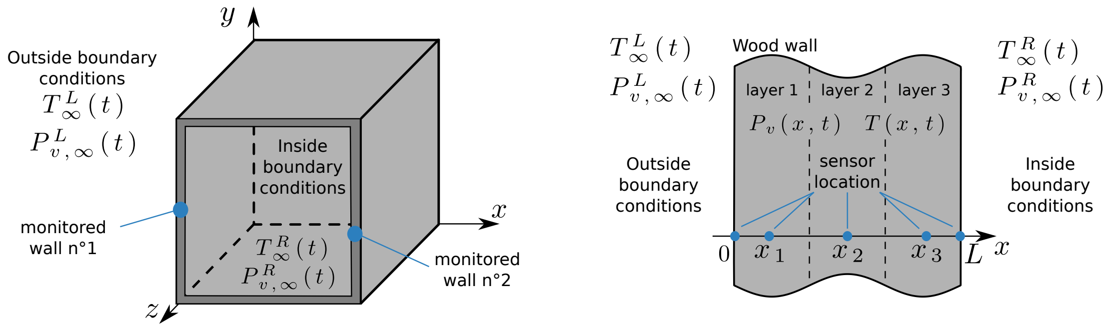

(a) (b)

Figure 2. *Illustration of the experimental set-up with the sensor locations.*

In terms of sensors, two walls are monitored as illustrated in Figure 2(a). A thermocouples (TC) is set on each inside and outside surfaces of the wall. As illustrated in Figure 2(b), three sensors are set inside the wall n°1 at the position x_1, x_2 and x_3, respectively. For the wall n°2, only one sensor is settled at the position x_2. The exact position is given in Table 1. The position uncertainty is $\sigma_x = 0.3\,\mathrm{cm}$ on the x-axis. The inside conditions are monitored with four TCs and four SHTs placed in a horizontal plane at $y = 0.44\,\mathrm{m}$. The outside boundary conditions are measured with a sensor placed $0.3\,\mathrm{m}$ above the cube. For each sensor, the time step between two consecutive measurements is set to 10 min.

Table 1. *Sensors positions within the walls.*

Wall	x_1 (cm)	x_2 (cm)	x_3 (cm)
n°1	1	3.44	4.08
n°2	-	3.44	-

5.2 Material properties

The material properties of the material come from [30]. The storage coefficients defined in Eq. (2) equals $c_{m,0} = 31.7\ \mathrm{kg/m^3}$, $c_{m,1} = -113.8\ \mathrm{kg/m^3}$, $c_{m,2} = 162\ \mathrm{kg/m^3}$ for the mass and $c_{q,0} = 630 \cdot 10^3\ \mathrm{J/(K \cdot m^3)}$, $c_{q,1} = 132.5 \cdot 10^3\ \mathrm{J/(K \cdot m^3)}$, $c_{q,2} = -237.8 \cdot 10^3\ \mathrm{J/(K \cdot m^3)}$, $c_{q,3} = 2.25.7 \cdot 10^3\ \mathrm{J/(K \cdot m^3)}$ for the heat. The diffusion coefficients from Eq. (3) are $k_{m,0} = 3 \cdot 10^{-13}\ \mathrm{s}$ and $k_{m,1} = 4.45 \cdot 10^{-12}\ \mathrm{s}$. The coefficient of variation of the heat diffusion coefficient with temperature in Eq. (4) is $k_{q,1} = 2 \cdot 10^{-4}\ \mathrm{W/(m \cdot K^2)}$. In the absence of data, the so-called thermo-diffusion coefficient is set to zero $k_{mq} = 0\ \mathrm{kg/(m \cdot s \cdot K)}$. The *a priori* value of the unknown parameters h_q^L, h_m^L, h_q^R, h_m^R, $k_{q,0,1}$, $k_{q,0,2}$ and $k_{q,0,3}$ are reported in Table 3.

5.3 Experimental observations

Before applying the forcing conditions to generate the experimental observations, the cube is set into an ambiance with constant temperature $T = 20.5$ °C and vapor pressure $P_v = 1100$ Pa for 30 days. The purpose is to ensure a steady state regime inside the walls before the carrying the experiments. Then, to generate the experimental observations used in the parameter estimation problem, the outside conditions are maintained constant around 20.5 °C and 1100 Pa. For the inside condition, an increase of temperature is imposed maintaining the relative humidity as constant (no source or sink). As a consequence, it leads to an increase of vapor pressure.

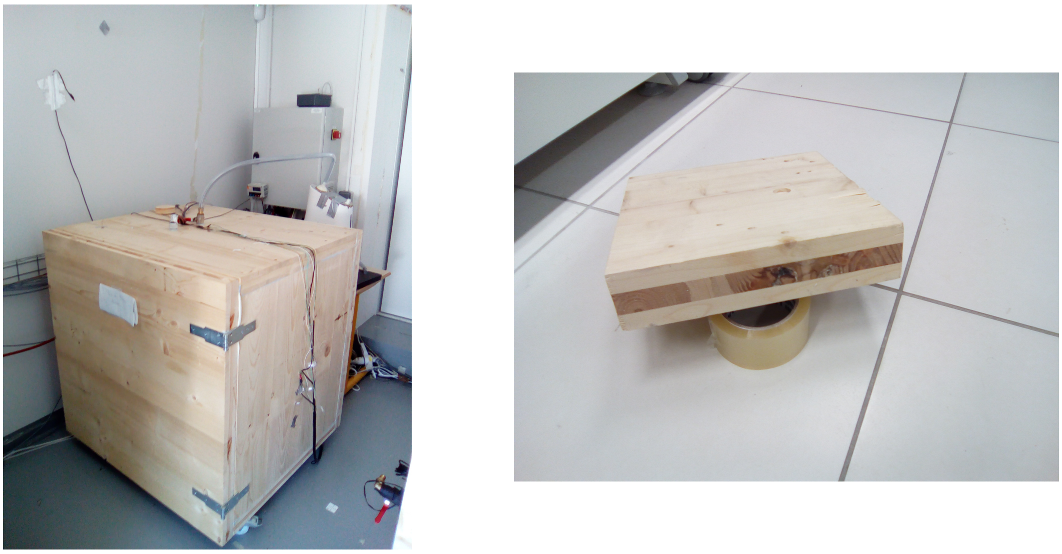

(a)

(b)

Figure 3. *Picture of the experimental set-up with the cube in the experimental chamber* (a) *and the CLT panel used* (b).

The total uncertainty on the observations are evaluated through the propagation of the uncertainties [31]. For the temperature, the total uncertainty is computed according to:

$$\sigma_T = \sqrt{\sigma_{m,T}^2 + \sigma_{x,T}^2 + \sigma_{t,T}^2}\,, \tag{13}$$

where $\sigma_{m,T} = 0.1\,^{\circ}\mathrm{C}$ is the measurement sensor uncertainty, $\sigma_{x,T}$ is the uncertainty due to the sensor location and σ_t is the one due to the response time of the sensor. The two last terms are given by:

$$\sigma_{x,T} = \frac{\partial T}{\partial x} \cdot \delta_x\,, \qquad \sigma_{t,T} = \frac{\partial T}{\partial t} \cdot \delta_t\,, \tag{14}$$

where $\delta_x = 0.3$ cm for the sensors located at $x \in \{x_1, x_2, x_3\}$, $\delta_x = 0.15$ cm for the sensors located at $x \in \{0, L\}$ and $\delta_t = 10$ min are the position uncertainty and the response time of the sensor. The term $\dfrac{\partial T}{\partial x}$ in Eq. (14) is evaluated at the location of the sensors using the numerical model and the *a priori* values of the unknown parameters. It should be noted that this term is not considered for the sensors in the ambient air. The second term $\dfrac{\partial T}{\partial t}$ is computed using the measurements and a discrete second order finite difference approach.

For the uncertainty on the vapor pressure, a similar procedure is adopted:

$$\sigma_P = \sqrt{\sigma_{m,P}^2 + \sigma_{x,P}^2 + \sigma_{t,P}^2}\,, \tag{15}$$

where the uncertainty due to the position and the response time are given by:

$$\sigma_{x,P} = \frac{\partial P_v}{\partial x} \cdot \delta_x\,, \qquad \sigma_{t,P} = \frac{\partial P_v}{\partial t} \cdot \delta_t\,.$$

The sensor measures the relative humidity and we have the following relation:

$$\partial P_v = P_{\mathrm{sat}} \cdot \partial \phi + \phi \cdot \frac{\partial P_{\mathrm{sat}}}{\partial T} \cdot \partial T\,.$$

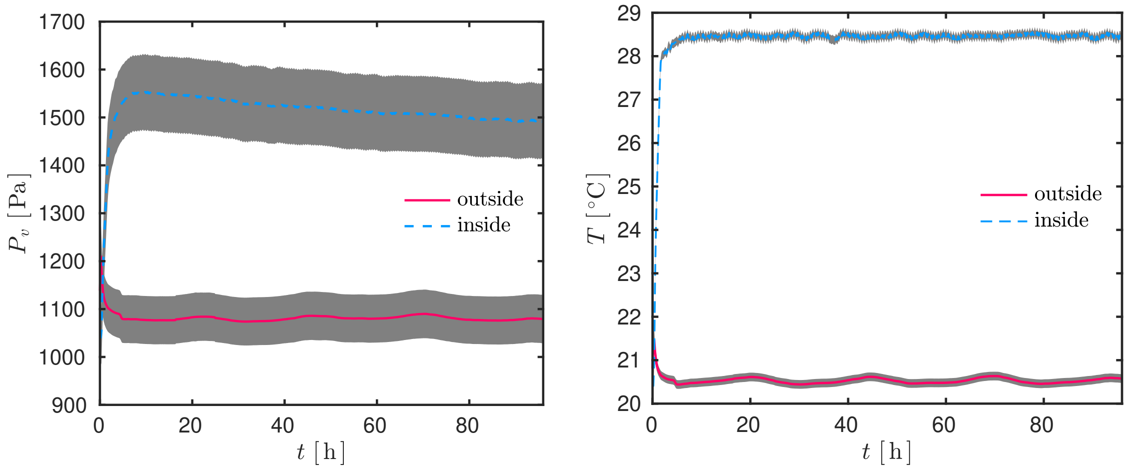

(a) (b)

Figure 4. *Variation of the boundary conditions for vapor pressure* (a) *and temperature* (b).

Thus, the measurement uncertainty of the vapor pressure is computed using the propagation relation:

$$\sigma_{m,P} = P_{\text{sat}}(T) \cdot \sigma_{m,\phi} + \frac{P_v \cdot r_v}{R_v \cdot T^2} \cdot \sigma_{m,T},$$

where $\sigma_{m,\phi} = 0.018$ ø is the uncertainty measurement from the sensor on relative humidity.

The boundary conditions are illustrated in Figures 4(a) and 4(b) with the uncertainty bounds. The uncertainties are higher for the vapor pressure than for temperature measurements. The uncertainty of the measurements are shown in Figures 5(a) and 5(b) for the sensor located at $x = x_3$. The contribution of each term in Eqs. (13) and (15) is highlighted. For the vapor pressure, the measurement uncertainty scales with $\mathcal{O}(65)$ Pa. Due to the sensor position, the uncertainty increases by $\mathcal{O}(5)$ Pa. It can be remarked that the time response of the sensor has almost no influence on the uncertainty propagation. For the temperature, the measurement uncertainty is 0.1 °C. With the sensor position, it increases to $\mathcal{O}(0.3)$ °C. The time response of the sensor has more influence, particularly at the beginning of the design where the variations are the most important. At $t = 1.5$ h, additional 0.2 °C are due to the time response in the total uncertainty.

The measured temperature and vapor pressure at $t = 0$ are illustrated in Figure 6 for the wall n°1. It can be assumed that the gradient of both fields is established. Thus, first order polynomial of $x \in [0, L]$ are fitted for each field:

$$T^0(x) = -6.825 \cdot x + 20.75 \; [\,{}^\circ\text{C}\,], \qquad P_v^0(x) = -502.7 \cdot x + 1087 \; [\text{Pa}].$$

Similarly, for the wall n°2, the fitted first order polynomial of x is

$$T^0(x) = 4.23 \cdot x + 19.93 \; [\,{}^\circ\text{C}\,], \qquad P_v^0(x) = -690.7 \cdot x + 1066 \; [\text{Pa}].$$

These interpolations are used as initial condition in the numerical model.

6 Results of the parameter estimation problem

6.1 Theoretical identifiability

The issue is first to demonstrate the theoretical identifiability of the unknown parameters. According to [21, 32], a parameter P is Structurally Globally Identifiable (SGI) in the model y

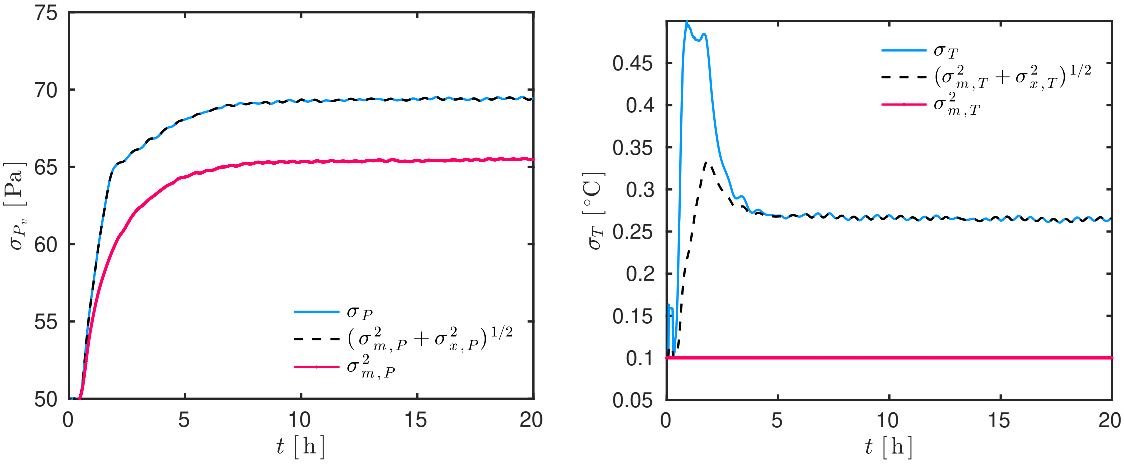

(a) (b)

Figure 5. *Variation of observations uncertainties for vapor pressure* (a) *and temperature* (b) *at* $x = x_3$.

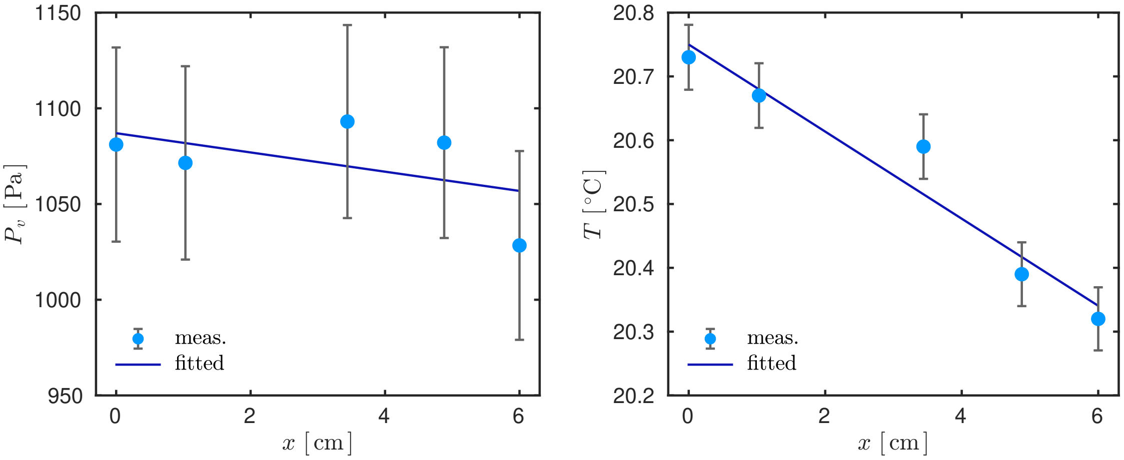

(a) (b)

Figure 6. *Profiles of measured and interpolated vapor pressure* (a) *and temperature* (b) *at* $t = 0$ *for the wall* n°1.

if the following condition is verified:

$$\forall \, (\, x \, , \, t \,) \, , \qquad y(\, P \,) \; = \; y(\, P' \,) \Longrightarrow P \; = \; P' \, .$$

This property is now evaluated for our model and the seven unknown coefficients $\mathrm{Bi}^{\,L}$, $\mathtt{Le}^{\,L}$, $\mathrm{Bi}^{\,R}$, $\mathtt{Le}^{\,R}$, $k_{\,q\,,0\,,1}$, $k_{\,q\,,0\,,2}$ and $k_{\,q\,,0\,,3}$. For the sake of clarity and without loss of generality, the subscript * is removed only in this subsection.

6.1.1 Parameters $k_{\,q\,,0\,,1}$, $k_{\,q\,,0\,,2}$ and $k_{\,q\,,0\,,3}$

The demonstration is first carried for the parameter $k_{\,q\,,0\,,1}$. A set of observable fields $u(\, x \; = \; x_{\,1} \, , \, t \,)$ and $v(\, x \; = \; x_{\,1} \, , \, t \,)$ is obtained with the parameter $k_{\,q\,,0\,,1}$. A second one is hold $u'(\, x \; = \; x_{\,1} \, , \, t \,)$ and $v'(\, x \; = \; x_{\,1} \, , \, t \,)$ according to the parameter $k'_{\,q\,,0\,,1}$. The point of observation $x_{\,1}$ is located in the first layer, so by definition:

$$k_{\,q}(\, x \; = \; x_{\,1} \, , \, u \,) \; = \; k_{\,q\,,0\,,1} \; + \; k_{\,q\,,1} \cdot u \, .$$

Thus, using the governing equation (5b) at the point of observation $x \; = \; x_{\,1}$, one can write for the first set of observable:

$$\begin{aligned} c_{\,q} \, (\, u \, , \, v \,) \cdot \frac{\partial v}{\partial t} \; = \; & \mathrm{Fo}^{\,q} \cdot \frac{\partial}{\partial x} \left(\, (\, k_{\,q\,,0\,,1} \; + \; k_{\,q\,,1} \cdot u \,) \cdot \frac{\partial v}{\partial x} \, \right) \\ & + \; \gamma \cdot \mathrm{Fo}^{\,q} \cdot r \, (\, v \,) \cdot \frac{\partial}{\partial x} \left(\, k_{\,m} \, (\, u \, , \, v \,) \cdot \frac{\partial u}{\partial x} \, \right) \end{aligned} \tag{16}$$

and for the second set:

$$\begin{aligned} c_{\,q} \, (\, u' \, , \, v' \,) \cdot \frac{\partial v'}{\partial t} \; = \; & \mathrm{Fo}^{\,q} \cdot \frac{\partial}{\partial x} \left(\, (\, k'_{\,q\,,0\,,1} \; + \; k_{\,q\,,1} \cdot u' \,) \cdot \frac{\partial v'}{\partial x} \, \right) \\ & + \; \gamma \cdot \mathrm{Fo}^{\,q} \cdot r \, (\, v' \,) \cdot \frac{\partial}{\partial x} \left(\, k_{\,m} \, (\, u' \, , \, v' \,) \cdot \frac{\partial u'}{\partial x} \, \right) \, . \end{aligned} \tag{17}$$

It is assumed that $u(\, x \, , \, t \,) \; \equiv \; u'(\, x \, , \, t \,)$ and $v(\, x \, , \, t \,) \; \equiv \; v'(\, x \, , \, t \,)$. We also have $\dfrac{\partial u}{\partial x} \; \equiv \; \dfrac{\partial u'}{\partial x}$ and $\dfrac{\partial v}{\partial x} \; \equiv \; \dfrac{\partial v'}{\partial x}$, $\dfrac{\partial^{\,2} u}{\partial x^{\,2}} \; \equiv \; \dfrac{\partial^{\,2} u'}{\partial x^{\,2}}$ and $\dfrac{\partial^{\,2} v}{\partial x^{\,2}} \; \equiv \; \dfrac{\partial^{\,2} v'}{\partial x^{\,2}}$ and $\dfrac{\partial u}{\partial t} \; \equiv \; \dfrac{\partial u'}{\partial t}$ and $\dfrac{\partial v}{\partial t} \; \equiv \; \dfrac{\partial v'}{\partial t}$. By carrying the operation Eq. (16) minus Eq. (17) and after some simplification, one obtains:

$$(\, k_{\,q\,,0\,,1} \; - \; k'_{\,q\,,0\,,1} \,) \cdot \frac{\partial^{\,2} v}{\partial x^{\,2}} \; = \; 0 \, .$$

It follows that:

$$k_{\,q\,,0\,,1} \; = \; k'_{\,q\,,0\,,1} \tag{18}$$

and the parameter $k_{\,q\,,0\,,1}$ is SGI. A very similar demonstration can be carried out to prove that the parameters $k_{\,q\,,0\,,2}$ and $k_{\,q\,,0\,,3}$ are SGI. It requires using the observable fields at $x \; = \; x_{\,2}$ for $k_{\,q\,,0\,,2}$ and $x \; = \; x_{\,3}$ for $k_{\,q\,,0\,,2}$, knowing that $x_{\,2}$ and $x_{\,3}$ are located in the second and third layers, respectively.

6.1.2 Parameters $\mathrm{Bi}^{\,L}$, $\mathtt{Le}^{\,L}$, $\mathrm{Bi}^{\,R}$ and $\mathtt{Le}^{\,R}$

The theoretical identifiability is now demonstrated for the parameters $\mathrm{Bi}^{\,L}$, $\mathtt{Le}^{\,L}$, $\mathrm{Bi}^{\,R}$ and $\mathtt{Le}^{\,R}$. A first set of observable fields $u(\, x \; = \; 0 \, , \, t \,)$ and $v(\, x \; = \; 0 \, , \, t \,)$, obtained with the set of parameters $\{ \, \mathrm{Bi}^{\,L} \, , \, \mathtt{Le}^{\,L} \, , \, \mathrm{Bi}^{\,R} \, , \, \mathtt{Le}^{\,R} \, , \, k_{\,q\,,0\,,1} \, \}$ is considered. A second one is also hold with $u'(\, x \; =$

$0\,,\,t\,)$ and $v'(\,x\,=\,0\,,\,t\,)$ related to the parameters $\{\,\mathrm{Bi}^{\,L\,\prime}\,,\,\mathtt{Le}^{\,L\,\prime}\,,\,\mathrm{Bi}^{\,R\,\prime}\,,\,\mathtt{Le}^{\,R\,\prime}\,,\,k'_{\,q\,,0\,,1}\,\}$. Using the boundary condition at $x\,=\,0$, defined in equation (6a), one can write:

$$k_{\,m}\cdot\frac{\partial u}{\partial x}\;+\;\delta\cdot\frac{\partial v}{\partial x}\;-\;\frac{\mathrm{Bi}^{\,L}}{\mathtt{Le}^{\,L}}\cdot\Big(\,u\;-\;u_{\,\infty}^{\,L}\,\Big)\;=\;k_{\,m}\cdot\frac{\partial u'}{\partial x}\;+\;\delta\cdot\frac{\partial v'}{\partial x}\;-\;\frac{\mathrm{Bi}^{\,L\,\prime}}{\mathtt{Le}^{\,L\,\prime}}\cdot\Big(\,u'\;-\;u_{\,\infty}^{\,L}\,\Big)\,. \tag{19}$$

Similarly, with equation (7a), it yields:

$$\big(\,k_{\,q\,,0\,,1}\;+\;k_{\,q\,,1}\cdot u\,\big)\cdot\frac{\partial v}{\partial x}\;+\;r\cdot\gamma\cdot k_{\,m}\cdot\frac{\partial u}{\partial x}\;-\;\mathrm{Bi}^{\,L}\cdot\Big(\,v\;-\;v_{\,\infty}^{\,L}\,\Big)\;+\;r\cdot\gamma\cdot\frac{\mathrm{Bi}^{\,L}}{\mathtt{Le}^{\,L}}\cdot\Big(\,u\;-\;u_{\,\infty}^{\,L}\,\Big) \tag{20}$$

$$\begin{aligned}=\;&\big(\,k'_{\,q\,,0\,,1}\;+\;k_{\,q\,,1}\cdot u'\,\big)\cdot\frac{\partial v'}{\partial x}\;+\;r\cdot\gamma\cdot k_{\,m}\cdot\frac{\partial u'}{\partial x}\;-\;\mathrm{Bi}^{\,L\,\prime}\cdot\Big(\,v'\;-\;v_{\,\infty}^{\,L}\,\Big)\\&\quad+\;r\cdot\gamma\cdot\frac{\mathrm{Bi}^{\,L\,\prime}}{\mathtt{Le}^{\,L\,\prime}}\cdot\Big(\,u'\;-\;u_{\,\infty}^{\,L}\,\Big)\,.\end{aligned}$$

Now, it is assumed that $u(\,x\,,\,t\,)\;\equiv\;u'(\,x\,,\,t\,)$ and $v(\,x\,,\,t\,)\;\equiv\;v'(\,x\,,\,t\,)$. Thus, we also have $\dfrac{\partial u}{\partial x}\equiv\dfrac{\partial u'}{\partial x}$ and $\dfrac{\partial v}{\partial x}\equiv\dfrac{\partial v'}{\partial x}$. Using this assumption and the results from Eq. (18), showing that parameter $k_{\,q\,,0\,,1}$ is SGI, equations (19) and (20) can be rewritten as:

$$\left(\,\frac{\mathrm{Bi}^{\,L}}{\mathtt{Le}^{\,L}}\;-\;\frac{\mathrm{Bi}^{\,L\,\prime}}{\mathtt{Le}^{\,L\,\prime}}\,\right)\cdot\Big(\,u'\;-\;u_{\,\infty}^{\,L}\,\Big)\;=\;0\,, \tag{21a}$$

$$\Big(\,\mathrm{Bi}^{\,L}\;-\;\mathrm{Bi}^{\,L\,\prime}\,\Big)\cdot\Big(\,v'\;-\;u_{\,\infty}^{\,L}\,\Big)\;+\;r\cdot\gamma\cdot\left(\,\frac{\mathrm{Bi}^{\,L}}{\mathtt{Le}^{\,L}}\;-\;\frac{\mathrm{Bi}^{\,L\,\prime}}{\mathtt{Le}^{\,L\,\prime}}\,\right)\cdot\Big(\,u'\;-\;u_{\,\infty}^{\,L}\,\Big)\;=\;0 \tag{21b}$$

By performing Eq. (21a) minus Eq. (21b), we have:

$$-\Big(\,\mathrm{Bi}^{\,L}\;-\;\mathrm{Bi}^{\,L\,\prime}\,\Big)\cdot\Big(\,v'\;-\;v_{\,\infty}^{\,L}\,\Big)\;=\;0\,,$$

Since v' and $v_{\,\infty}^{\,L}$ are independent, it produces:

$$\mathrm{Bi}^{\,L}\;=\;\mathrm{Bi}^{\,L\,\prime}$$

and the parameter $\mathrm{Bi}^{\,L}$ is SGI. Using this result and equation. (21a), we obtain:

$$r\cdot\gamma\cdot\mathrm{Bi}^{\,L}\cdot\left(\,\frac{1}{\mathtt{Le}^{\,L}}\;-\;\frac{1}{\mathtt{Le}^{\,L\,\prime}}\,\right)\cdot\Big(\,u'\;-\;u_{\,\infty}^{\,L}\,\Big)\;=\;0\,.$$

Again, since u' and $u_{\,\infty}^{\,L}$ are independent it returns that:

$$\mathtt{Le}^{\,L}\;=\;\mathtt{Le}^{\,L\,\prime}$$

and the parameter $\mathtt{Le}^{\,L}$ is SGI. A very similar demonstration can be performed using the boundary conditions (6b) and (7b) and the observable fields $u(\,x\,=\,1\,,\,t\,)$ and $v(\,x\,=\,1\,,\,t\,)$ to prove that the parameters $\{\,\mathrm{Bi}^{\,R}\,,\,\mathtt{Le}^{\,R}\,\}$ are SGI.

It is important to remark that the seven parameters $\mathrm{Bi}^{\,L}$, $\mathtt{Le}^{\,L}$, $\mathrm{Bi}^{\,R}$, $\mathtt{Le}^{\,R}$, $k_{\,q\,,0\,,1}$, $k_{\,q\,,0\,,2}$ and $k_{\,q\,,0\,,3}$ are theoretically identifiable because the experimental design enables to obtain two observable fields at the boundaries $x\;=\;\{\,0\,,\,1\,\}$ and one measurement in each material $x\;=\;\{\,x_{\,1}\,,\,x_{\,2}\,,\,x_{\,3}\,\}$. Indeed, the demonstration for $k_{\,q\,,0\,,1}$ is realized using the governing equation (5b) at the point of observation $x_{\,1}$. The proof of identifiability is obtained because $x_{\,1}$ is located in the material 1, which thermal property $k_{\,q\,,0\,,1}$ is unknown. In addition, the proof for the parameters $\mathrm{Bi}^{\,L}$, $\mathtt{Le}^{\,L}$, $\mathrm{Bi}^{\,R}$ and $\mathtt{Le}^{\,R}$ is obtained using the result of identifiability of the parameter $k_{\,q\,,0\,,1}$ from Eq. (18). Without these conditions, the theoretical identifiability could not be demonstrated.

6.2 Practical identifiability

The computation of the sensitivity equation is realised using the numerical model described in Section 3 and the discretisation parameters $\Delta t \;=\; 36$ s and $\Delta x \;=\; 6 \cdot 10^{-2}$ cm. The *a priori* values of the unknown parameters, reported in Table 3 are used.

The time evolution of the sensitivity coefficients of the four parameters $\mathrm{Bi}^{\,L}$, $\mathtt{Le}^{\,L}$, $\mathrm{Bi}^{\,R}$ and $\mathtt{Le}^{\,R}$ are shown in Figure 7. Several results can be observed. First, for both fields u and v, the magnitude of the sensitivity functions are higher for the right Biot numbers $\mathrm{Bi}^{\,R}$ than for the left one $\mathrm{Bi}^{\,L}$, as noticed in Figures 7(a)–7(d). It is consistent since the forcing conditions occurs at the right boundary according to the experimental design shown in Figures 4(a) and 4(b).

Secondly, for $\mathrm{Bi}^{\,L}$ and $\mathtt{Le}^{\,L}$, the magnitudes of the sensitivity functions are maximal at $x \;=\; 0$. The model is the more sensible to these parameters at the boundary $x \;=\; 0$. It is corroborated by the fact that these parameters influence the model through the boundary condition defined in Eqs. (7a) and (6a). Similar remarks can be done for the parameters $\mathrm{Bi}^{\,R}$ and $\mathtt{Le}^{\,R}$.

By comparing qualitatively the sensitivity functions for Biot and Lewis parameters, it can be noted that the variations are very poor for the $\mathtt{Le}^{\,L}$ and $\mathtt{Le}^{\,R}$. It indicated that the estimation of these parameters may be less accurate.

The variation of the criteria Ψ as a function of the number of measurement are shown in Figure 8(a). As expected, it increases with the number of measurement considered. The optimal design is obtained when using the five measurements for the parameter estimation problem. In Figure 8(b), the variation of the criteria Ψ according to the time length of the experimental design is given. The criteria reaches it maximal around $t \;=\; 5$ h. This peak corresponds to the increase of temperature and vapor pressure in the material. After $t \;=\; 20$ h, the criteria Ψ scales with 0. It coincides with the reach of the quasi-steady state in the process as noted in Figure 9. These results reveals that it is not necessary to increase the duration of the experiment to ensure the maximum accuracy when estimating the unknown parameters.

The correlation between the sensitivity functions are given in Table 2. It is computed from the Jacobian matrix. The correlation between the couple of unknown parameters $\bigl(\,\mathrm{Bi}^{\,L},\, k^{\,\star}_{\,q\,,0\,,1}\,\bigr)$, $\bigl(\,\mathrm{Bi}^{\,R},\, k^{\,\star}_{\,q\,,0\,,2}\,\bigr)$, $\bigl(\,\mathrm{Bi}^{\,L},\, \mathtt{Le}^{\,L}\,\bigr)$ and $\bigl(\,\mathrm{Bi}^{\,R},\, \mathtt{Le}^{\,R}\,\bigr)$ is reduced by using multiple observations at different points in the material. One may conclude that all the unknown parameters are identifiable from a practical point of view.

Table 2. *Correlation between the sensitivity coefficients.*

	for u							for v						
	$\mathrm{Bi}^{\,L}$	$\mathtt{Le}^{\,L}$	$\mathrm{Bi}^{\,R}$	$\mathtt{Le}^{\,R}$	$k^{\,\star}_{\,q\,,0\,,1}$	$k^{\,\star}_{\,q\,,0\,,2}$	$k^{\,\star}_{\,q\,,0\,,3}$	$\mathrm{Bi}^{\,L}$	$\mathtt{Le}^{\,L}$	$\mathrm{Bi}^{\,R}$	$\mathtt{Le}^{\,R}$	$k^{\,\star}_{\,q\,,0\,,1}$	$k^{\,\star}_{\,q\,,0\,,2}$	$k^{\,\star}_{\,q\,,0\,,3}$
$\mathrm{Bi}^{\,L}$	1	−0.3	−0.03	0.7	0.5	−0.4	−0.5	1	−0.3	−0.8	−0.5	−0.4	−0.7	−0.4
$\mathtt{Le}^{\,L}$		1	−0.7	0.5	0.6	0.5	−0.4		1	−0.1	−0.2	−0.1	0.2	0.3
$\mathrm{Bi}^{\,R}$			1	−0.2	−0.7	−0.8	0.6			1	−0.4	−0.5	−0.8	−0.4
$\mathtt{Le}^{\,R}$				1	−0.2	0.3	0.4				1	0.3	0.4	−0.02
$k^{\,\star}_{\,q\,,0\,,1}$					1	0.5	−0.8					1	0.5	−0.4
$k^{\,\star}_{\,q\,,0\,,2}$						1	−0.3						1	0.08
$k^{\,\star}_{\,q\,,0\,,3}$							1							1

6.3 Parameter estimation

The parameter estimation problem is solved using the optimization procedure described in Section 4.2 and the direct numerical model detailed in Section 3. The discretisation parameters are set to $\Delta t \;=\; 36$ s and $\Delta x \;=\; 6 \cdot 10^{-2}$ cm. In this way, one direct computation of the numerical model requires 12 s, which corresponds to a ratio of $R_{\mathrm{cpu}} \;=\; 0.13$ s/h of physical simulation. The evolution of the cost function and its gradient according to the iterations is given

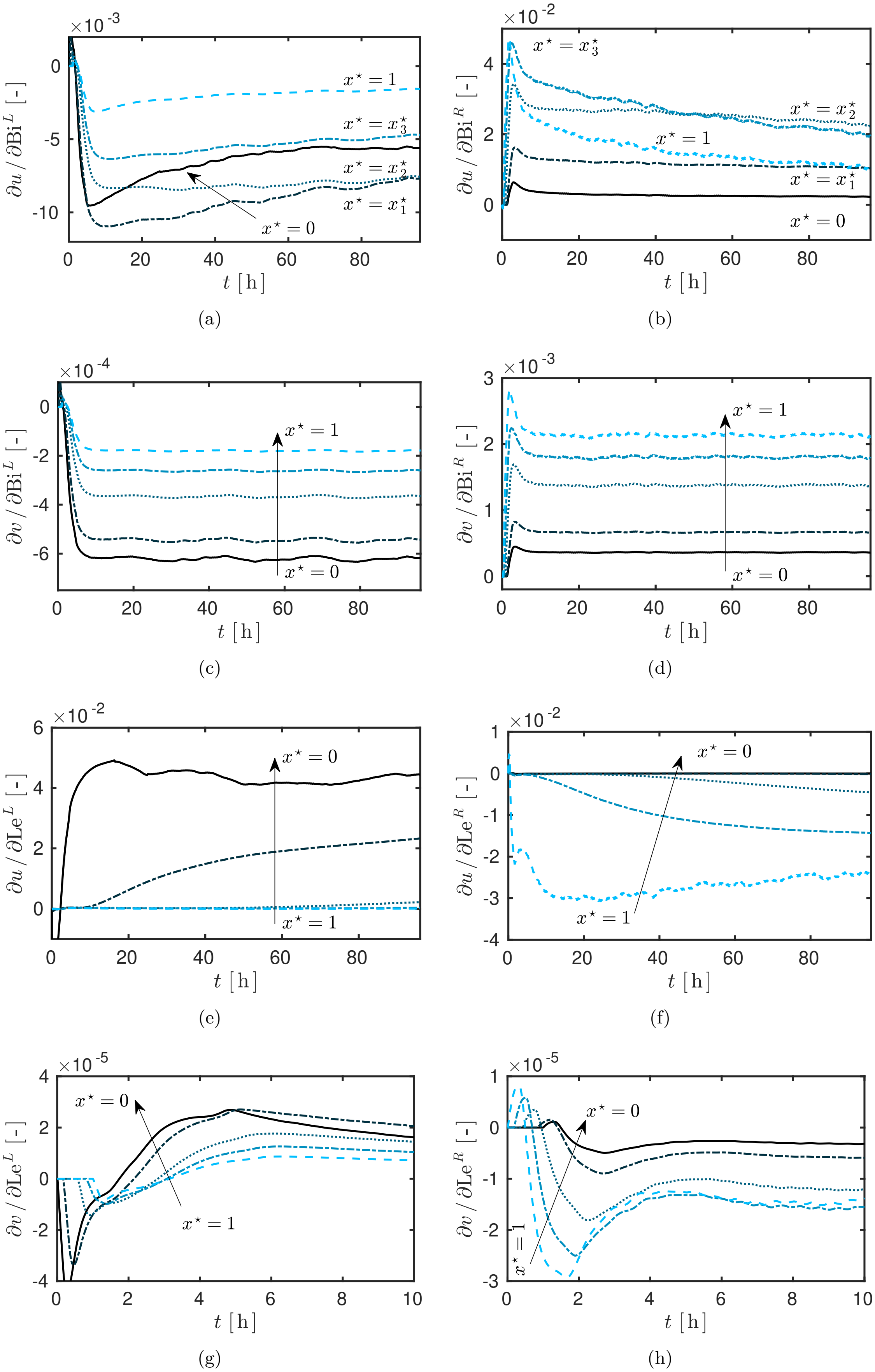

Figure 7. *Time evolution of the sensitivity coefficients of the parameters* $\mathrm{Bi}^{\,L}$ (a,c), $\mathrm{Bi}^{\,R}$ (b,d), $\mathtt{Le}^{\,L}$ (e,g) *and* $\mathtt{Le}^{\,R}$ (f,h) *at the measurements points* $x^\star \in \{\,0\,,\, x_1^\star\,,\, x_2^\star\,,\, x_3^\star\,,\, 1\,\}$ *for vapor pressure* (a,b,e,f) *and temperature* (c,d,g,h).

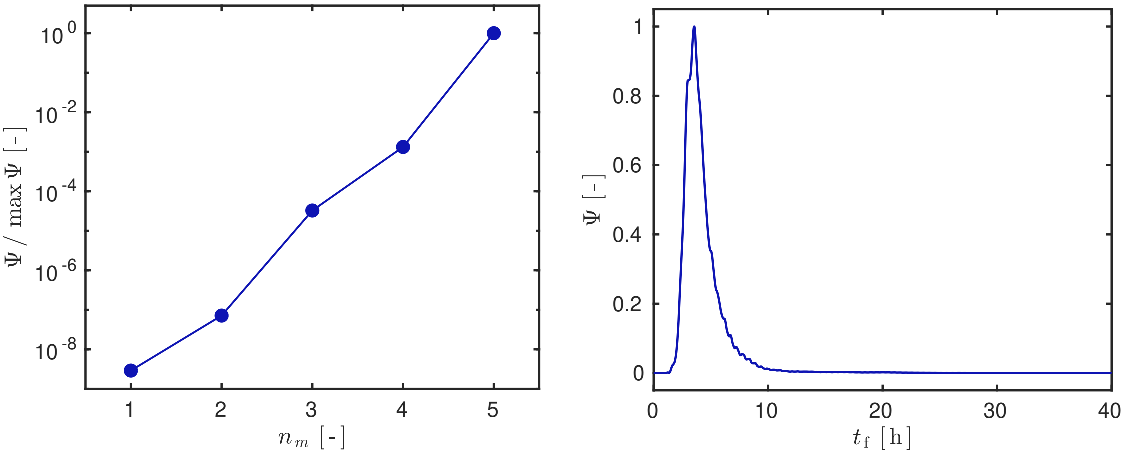

(a) (b)

Figure 8. *Variation of the criteria Ψ according to the number of measurement* (a) *and to the time length of the experimental design* (b)*.*

in Figures 11(a) and 11(b). Around 100 iterations are required for the algorithm to estimate the parameters.

The estimated parameter after optimization are reported in Table 3. The value of the parameter is in accordance with the physical expectations. As mentioned in [2, 33], the heat and mass surface coefficients scales with this order of magnitude. The heat surface coefficient is higher for the left boundary. Indeed the left boundary is in contact with the climatic chamber. The convective heat transfer are probably higher in the climatic chamber than inside the cube. Using the estimated parameter $k_{q,0,i}$, it corresponds to a thermal conductivity of 0.14 W/(m · K), 0.12 W/(m · K) and 0.09 W/(m · K) at 20 °C for the layers 1, 2 and 3, respectively. This values are consistent with the thermal conductivity of spruce measured and reported in [34, 35].

The error estimator of the parameters at the left boundary h_q^L and h_m^L is particularly high. It is due to a low magnitudes of the sensitivity coefficients of the Biot numbers at this boundary as noticed when comparing Figures 7(a)–7(d). For the other parameters, the uncertainty is very satisfactory, being at least one order lower than the parameter value.

Figure 9 shows a comparison between the experimental observations and the numerical predictions obtained with the seven estimated parameters Bi^{L}, $\mathtt{Le}^{L}$, Bi^{R}, $\mathtt{Le}^{R}$, $k_{q,0,1}^{\star}$, $k_{q,0,2}^{\star}$ and $k_{q,0,3}^{\star}$. A satisfactory agreement is remarked for all points of observations. The predictions remains in the uncertainty band of the measurements. Some little discrepancies are noted for the temperature field at $x = x_3$. The residual between the numerical computations and the experiments are shown in Figures 10(a) and 10(b) for vapor pressure and temperature, respectively. The residuals are signed particularly at the beginning of the experiments $t \in [0, 10]$ h, indicating that some physical phenomena may be omitted in the description of the mathematical model. Despite these observations, the residuals remain under the uncertainty of the measurement as deduced from Figure 13 showing the probability density function of the relative residuals. For the sake of compactness, the probability density function are only presented for $x = x_2$ and $x = L$.

7 Evaluating the reliability of the mathematical model

To evaluate the reliability of the mathematical model with the estimated parameters, the numerical predictions are compared with other experimental observations. The latter is obtained in the wall n °2 of the cube shown in Figure 2(a). The numerical model is used to compute the

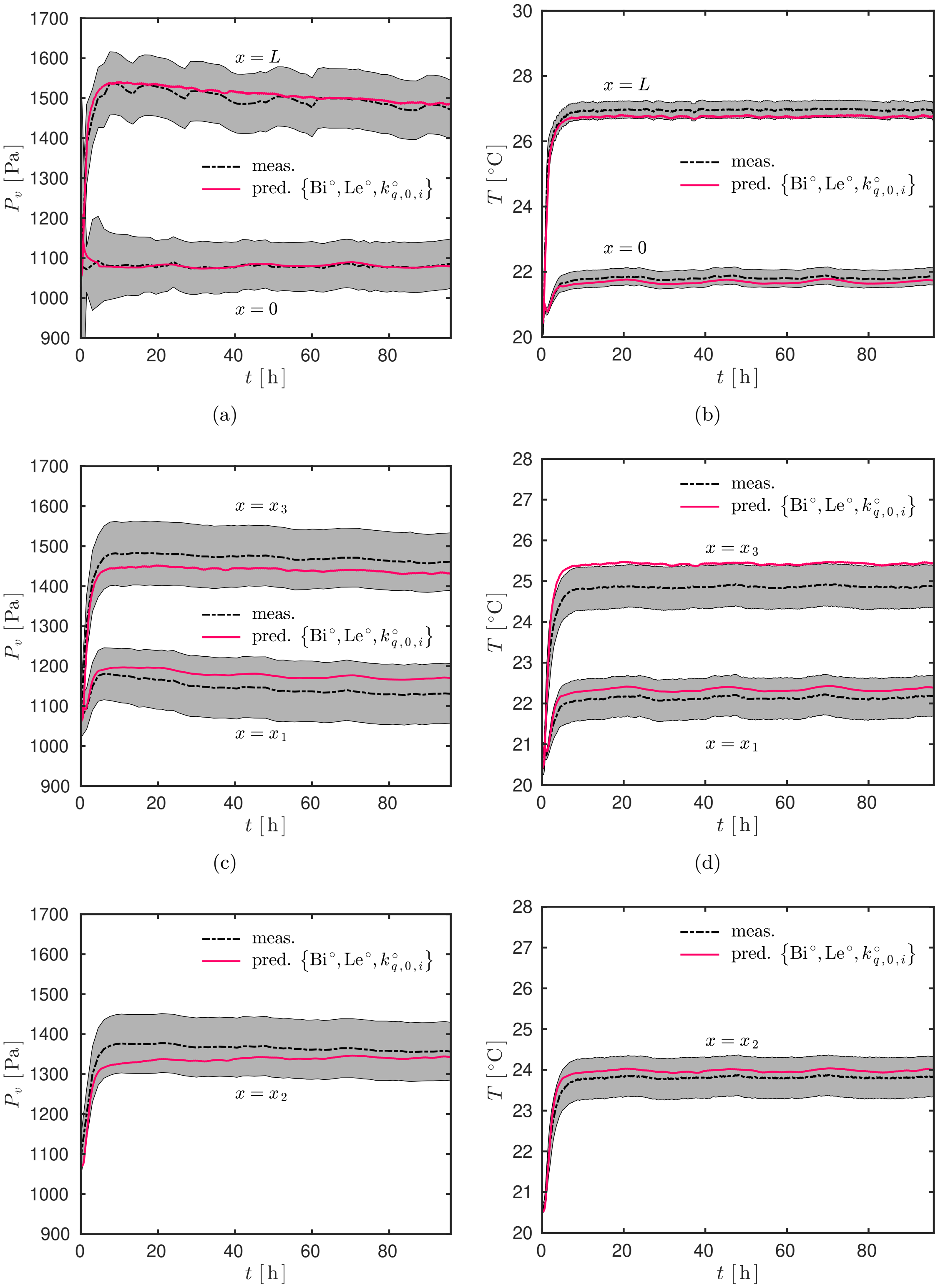

(a) (b)

(c) (d)

(e) (f)

Figure 9. *Comparison between the numerical predictions with the estimated parameters* Bi^{L}, $\mathtt{Le}^{L}$, Bi^{R}, $\mathtt{Le}^{R}$, $k_{q,0,1}$, $k_{q,0,2}$ *and* $k_{q,0,3}$ *and the experimental observations for vapor pressure* (a,c,e) *and temperature* (b,d,f).

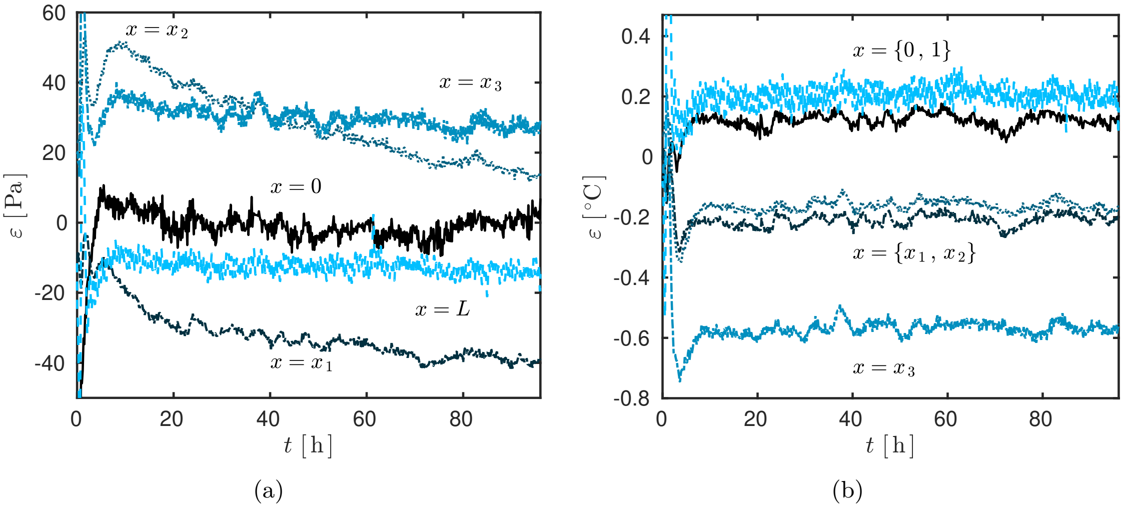

Figure 10. *Residual between the numerical predictions and the experimental observations for vapor pressure* (a) *and temperature* (b).

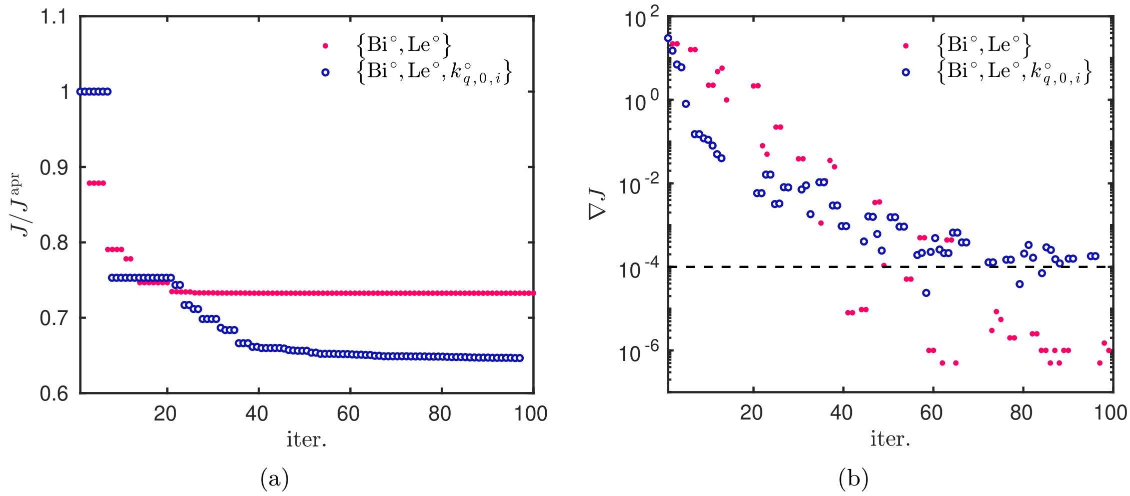

Figure 11. *Convergence of the optimisation process: evolution of the cost function* (a) *and its variation* (b) *with the number of iterations.*

Table 3. *Values of the unknown parameters.*

	A priori value	Estimated $\Omega_p = \{\mathrm{Bi}, \mathtt{Le}, k_{q,0,i}\}$		Estimated $\Omega_p = \{\mathrm{Bi}, \mathtt{Le}\}$	
Parameter	p_k^{apr}	p_k°	Error estimator ϵ_k	p_k°	Error estimator ϵ_k
h_q^L $\left[\mathrm{W/(m^2 \cdot K)}\right]$	10	7.76	± 0.3	8.21	± 0.1
h_m^L $\left[\mathrm{m^2/(K \cdot s)}\right]$	$7.6 \cdot 10^{-6}$	$2.8 \cdot 10^{-6}$	$\pm 4 \cdot 10^{-5}$	$2.6 \cdot 10^{-8}$	$\pm 9 \cdot 10^{-9}$
h_q^R $\left[\mathrm{W/(m^2 \cdot K)}\right]$	5	6.4	$\pm 2 \cdot 10^{-3}$	7.2	$\pm 7 \cdot 10^{-3}$
h_m^R $\left[\mathrm{m^2/(K \cdot s)}\right]$	$3.7 \cdot 10^{-6}$	$1.1 \cdot 10^{-9}$	$\pm 8 \cdot 10^{-10}$	$2.7 \cdot 10^{-6}$	$\pm 2 \cdot 10^{-7}$
$k_{q,0,1}$ $\left[\mathrm{W/(m \cdot K)}\right]$	$6.3 \cdot 10^{-2}$	$8.2 \cdot 10^{-2}$	$\pm 2 \cdot 10^{-3}$	-	-
$k_{q,0,2}$ $\left[\mathrm{W/(m \cdot K)}\right]$	$6.3 \cdot 10^{-2}$	$6.9 \cdot 10^{-2}$	$\pm 1 \cdot 10^{-3}$	-	-
$k_{q,0,3}$ $\left[\mathrm{W/(m \cdot K)}\right]$	$6.3 \cdot 10^{-2}$	$3.1 \cdot 10^{-2}$	$\pm 1 \cdot 10^{-4}$	-	-

solution with the discretisation parameters set to $\Delta t = 36$ s and $\Delta x = 6 \cdot 10^{-2}$ cm. The material properties are detailed in Section 5.2. For the unknown parameters h_q^L, h_m^L, h_q^R, h_m^R and $k_{q,0,i}, i = \{1, 2, 3\}$, the estimated values reported in Table 3 are used. The boundary and initial conditions are given in Section 5.3.

Figure 12 compares the numerical predictions with the experimental observations. A very satisfactory agreement is observed between both results. A small discrepancy is observed for the temperature at $x = 0$. As mentioned before, the Biot and Lewis numbers at this boundary have been determined with low confidence. Thus, additional experimental observations should be generated using, for instance, forcing conditions at the boundary $x = 0$, to estimate with better accuracy these two parameters.

To discuss further the robustness of the mathematical model, two hypothesis are now discussed. First, the importance of the coupling term $c_{mq} \cdot \dfrac{\partial T}{\partial t}$ in Eq. (1a) is evaluated. For this, using the estimated values of the seven unknown parameters reported in Table 3, an additional computation of the direct model is performed setting to zero the coupling parameter $\eta = 0$. The impact of the coupling term is observed in Figures 13(a) and 13(b). As expected, when vanishing, the prediction of the temperature almost do not change since the coupling term affects the mass transport equation (1a). However, the relative error on the prediction scales with -20% for the vapor pressure at $x = x_2$. Thus, omitting this term in the mass transport equation leads to an important underestimation of the vapor diffusion process in the material.

The second hypothesis analyzed concerns the assumption of a different thermal conductivity for each layer of the CLT panels. Figures 14(a) and 14(b) compares the numerical predictions with the experimental measurements in the wall n°1 at the quasi-steady state regime $t = 96$ h. For vapor pressure, the hypothesis of considering a constant in space vapor diffusion is acceptable since the slope of vapor pressure do not vary much according to space. On the contrary, for temperature, the experimental measurement seems to highlight three different slopes for each layer. Using the estimated parameters, the direct model predicts three distinct profiles of temperature in each layer. Additional computations are carried out considering a direct model with a constant in space thermal conductivity equal to the *a priori* value $k_{q,0,i} = 6.3 \cdot 10^{-2}$ $\mathrm{W/(m \cdot K)}, i = \{1, 2, 3\}$. The unknown Biot and Lewis numbers are then estimated using the same optimization procedure. Results are reported in Table 3 in the column "Estimated $\Omega_p = \{\mathrm{Bi}, \mathtt{Le}\}$". As shown in Figures 13(c) and 13(d), the prediction of the fields at the surface $x = L$ are not changed compared to the previous optimization results. However, discrepancies in the predictions appear at $x = x_2$ as shown in Figures 13(a) and 13(b). This discrepancies can also be remarked in Figure 14(b) for the measurement inside the material. In addition, Figure 11(a) reports that the cost function is higher for the case searching only for the Biot and Lewis numbers. Thus, one may conclude on the importance of modeling the heat

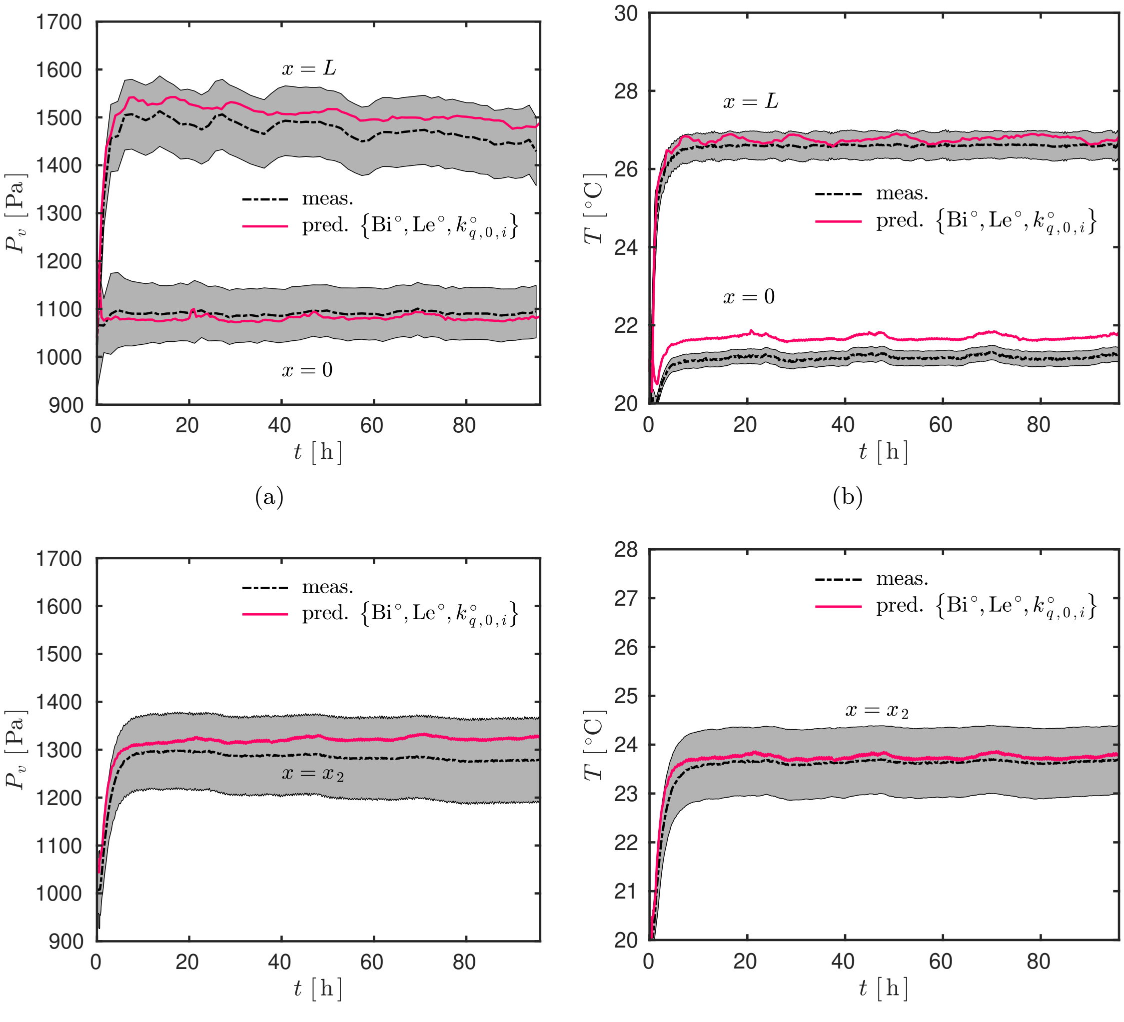

(a) (b)

(c) (d)

Figure 12. *Comparison between the numerical prediction with the estimated parameters* Bi^{L}, $\mathtt{Le}^{L}$, Bi^{R}, $\mathtt{Le}^{R}$, $k_{q,0,1}$, $k_{q,0,2}$ *and* $k_{q,0,3}$ *and experimental observations from another wall for vapor pressure* (a,c,e) *and temperature* (b,d,f).

transfer process by considering a space dependent thermal conductivity according to each layer. Without this assumption, the prediction of the model are reliable only at the boundaries.

8 Conclusion

The reliability of a numerical model is a crucial feature to predict the physical phenomena with accuracy. Several works in the literature proposed an evaluation of the robustness of models for heat and mass transfer in porous material by comparing the numerical predictions to experimental observations. Nevertheless, two major sources of error are identified. First, the heat and mass surface transfer coefficients, which are generally assumed using empirical correlations. The second source raises from the material properties which are determined using the standard methods with experimental data obtained in steady-state regime.

To faces this challenge, the article proposed to evaluate the reliability of a model for an hygroscopic material, reducing these sources of uncertainty. After presenting the mathematical model of heat and mass transfer in Section 2, Section 3 detailed the numerical model to compute the solution of the governing equations. It is based on an explicit unconditionally

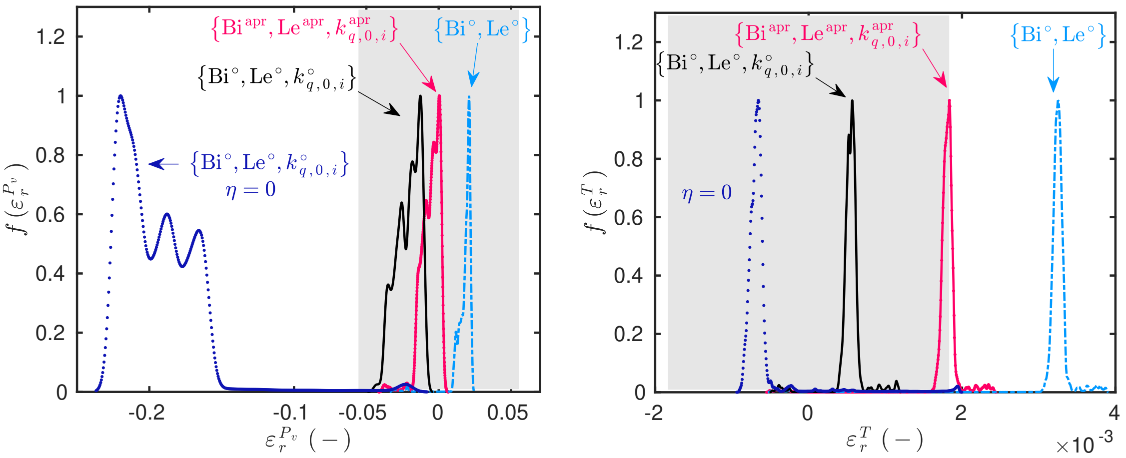

(a) $x = x_2$

(b) $x = x_2$

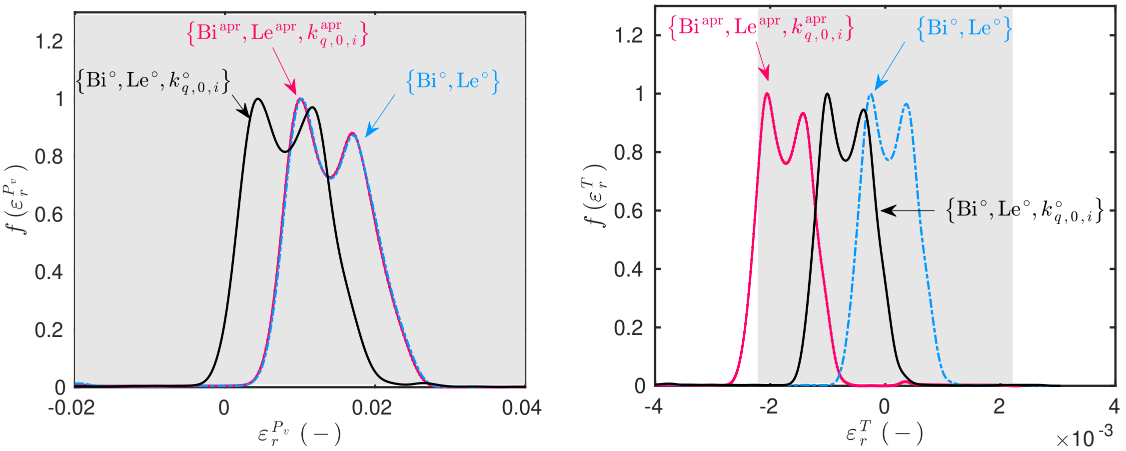

(c) $x = L$

(d) $x = L$

Figure 13. *Probability density function of the relative residual between the experimental observations and the numerical predictions for vapor pressure* (a,c) *and temperature* (b,d). *The grey shadow represents the band of measurement uncertainty.*

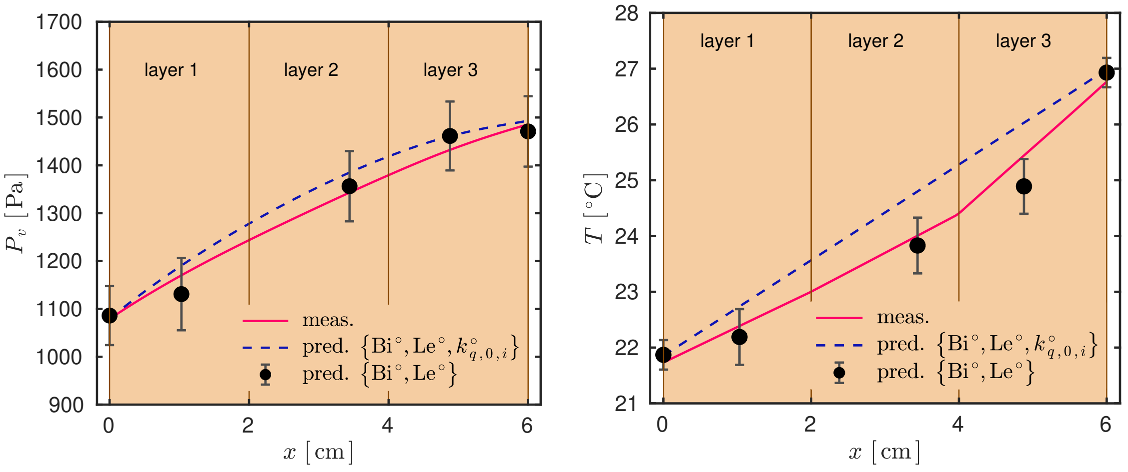

(a)

(b)

Figure 14. *Comparison between the numerical predictions and the experimental observations for vapor pressure* (a) *and temperature* (b) *at the quasi-steady state regime* $t = 96$ *h*.

stable numerical scheme. It permits to avoid costly subiterations at each time iterations to treat the non-linearities of the problem. Furthermore, the stability condition of the standard Euler explicit approach can be relaxed to reduce the computational efforts. This feature is particularly important in the framework of parameter estimation problem. The experimental facility is composed of an enclosure made with spruce CLT panels. The inside and outside air volumes temperature and vapor pressure can be controlled. Two walls of the small cube are monitored using sensors. The experimental observations are generated by forcing an increase of temperature in the inside air volumes. It induces a diffusion process of heat and mass from the inner to the outer parts of the walls.

In Section 6, a first set composed of five experimental observations is used to estimate seven unknown parameters in the model, namely the heat and mass surface transfer coefficients and the thermal conductivity of each of the three layers. The theoretical identifiability of the unknown parameters is demonstrated. It appears that the seven parameters are identifiable only because the experimental design provides five measurements, located at the boundaries and in each layer of the wall. Then, the practical identifiability is verified by computing the sensitivity coefficients of each parameter. Last, the results of the parameter estimation problem are presented. The physical values of the parameters are in accordance with several references from the literature. The use of hybrid optimizer ensures an estimation in less than 60 iterations.

Last, the reliability of the model is evaluated by comparing the numerical prediction to a second set of experimental observations obtained in another wall for the same forcing conditions. A very satisfactory prediction is observed highlighting the good reliability of the model. The importance of the coupling between heat and mass transfer is discussed. Furthermore, the importance of considering a space-dependent thermal conductivity is shown. It indicates that the standard methods to determine this material property is questionable for such hygroscopic material.

In this work, the experimental observations are generated through an increase in temperature. The driven process is heat transfer. Further works should focus on generating additional experimental observations by forcing the mass transfer through the material. It will require to improve the mathematical model by integrating the hysteresis effects on the sorption curve, which are particularly important for such materials.

Acknowledgments

The authors acknowledge the Junior Chair Research program “Building performance assessment, evaluation and enhancement” from the University of Savoie Mont Blanc in collaboration with The French Atomic and Alternative Energy Center (CEA) and Scientific and Technical Center for Buildings (CSTB). The authors thanks the grants from the Carnot Institute “Energies du Futur” through the project MN4BAT. The authors gratefully acknowledge the financial support from Florida International University in the form of an FIU Presidential Fellowship and FIU Dissertation Year Fellowship.

References

[1] A.V. Luikov. *Heat and Mass Transfer in Capillary-Porous Bodies.* Pergamon, Oxford, 1966. 4, 6

[2] N. Mendes, M. Chhay, J. Berger, and D. Dutykh. *Numerical methods for diffusion phenomena in building physics.* PUCPress, Curitiba, Brazil, 2016. 4, 22

[3] T. Kalamees and J. Vinha. Hygrothermal calculations and laboratory tests on timber-framed wall structures. *Building and Environment*, 38(5):689–697, 2003. 4

[4] J. Berger, D. Dutykh, N. Mendes, and B. Rysbaiuly. A new model for simulating heat, air and moisture transport in porous building materials. *International Journal of Heat and Mass Transfer*, 134:1041–1060, 2019. 4

[5] D. Lelievre, T. Colinart, and P. Glouannec. Hygrothermal behavior of bio-based building materials including hysteresis effects: Experimental and numerical analyses. *Energy and Buildings*, 84:617–627, 2014. 4

[6] T. Defraeye, B. Blocken, D. Derome, B. Nicolai, and J. Carmeliet. Convective heat and mass transfer modelling at air–porous material interfaces: Overview of existing methods and relevance. *Chemical Engineering Science*, 74:49–58, 2012. 4

[7] J. Carmeliet and D. Derome. Temperature driven inward vapor diffusion under constant and cyclic loading in small-scale wall assemblies: Part 1 experimental investigation. *Building and Environment*, 48:48–56, 2012. 4

[8] J. Carmeliet and D. Derome. Temperature driven inward vapor diffusion under constant and cyclic loading in small-scale wall assemblies: Part 2 heat-moisture transport simulations. *Building and Environment*, 47:161–169, 2012. 4

[9] P. Talukdar, S.O. Olutmayin, O.F. Osanyintola, and C.J. Simonson. An experimental data set for benchmarking 1-d, transient heat and moisture transfer models of hygroscopic building materials. part i: Experimental facility and material property data. *International Journal of Heat and Mass Transfer*, 50(23–24):4527–4539, 2007. 4

[10] P. Talukdar, O.F. Osanyintola, S.O. Olutimayin, and C.J. Simonson. An experimental data set for benchmarking 1-d, transient heat and moisture transfer models of hygroscopic building materials. part II: Experimental, numerical and analytical data. *International Journal of Heat and Mass Transfer*, 50(25-26):4915–4926, 2007. 4

[11] C. James, C. J. Simonson, P. Talukdar, and S. Roels. Numerical and experimental data set for benchmarking hygroscopic buffering models. *International Journal of Heat and Mass Transfer*, 53(19–20):3638–3654, 2010. 4

[12] M. Steeman, M. Van Belleghem, M. De Paepe, and A. Janssens. Experimental validation and sensitivity analysis of a coupled BES–HAM model. *Building and Environment*, 45(10):2202–2217, 2010. 4

[13] T. Busser, J. Berger, A. Piot, M. Pailha, and M. Woloszyn. Comparison of model numerical predictions of heat and moisture transfer in porous media with experimental observations at material and wall scales: an analysis of recent trends. *Drying Technology*, 0(0):1–33, 2018. 4

[14] P. Perre, A. Challansonnex, and J. Colin. On the importance of heat and mass transfer coupling for the characterization of hygroscopic insulation materials. *International Journal of Heat and Mass Transfer*, 133:968–975, 2019. 4

[15] E. C. Du Fort and S. P. Frankel. Stability conditions in the numerical treatment of parabolic differential equations. *Mathematical Tables and Other Aids to Computation*, 7(43):135–152, 1953. 9

[16] S. Gasparin, J. Berger, D. Dutykh, and N. Mendes. Stable explicit schemes for simulation of nonlinear moisture transfer in porous materials. *Journal of Building Performance Simulation*, 11(2):129–144, 2018. 9

[17] S. Gasparin, J. Berger, D. Dutykh, and N. Mendes. An improved explicit scheme for whole-building hygrothermal simulation. *Building Simulation*, 11(3):465–481, 2018. 9

[18] R. Courant, K. Friedrichs, and H. Lewy. Über die partiellen Differenzengleichungen der mathematischen Physik. *Mathematische Annalen*, 100(1):32–74, 1928. 9

[19] M. Necati Ozisik and H. R.B. Orlande. *Inverse Heat Transfer: Fundamentals and Applications*. CRC Press, New York, 2000. 11

[20] J. V. Beck and K. J. Arnold. *Parameter Estimation in Engineering and Science*. John Wiley and Sons, New York, 1977. 11

[21] E. Walter and L. Pronzato. Qualitative and quantitative experiment design for phenomenological models; a survey. *Automatica*, 26(2):195–213, 1990. 12, 13, 16

[22] D. Ucinski. *Optimal Measurement Methods for Distributed Parameter System Identification*. CRC Press, New York, 2004.

[23] M. Karalashvili, W. Marquardt, and A. Mhamdi. Optimal experimental design for identification of transport coefficient models in convection–diffusion equations. *Computers and Chemical Engineering*, 80:101–113, 2015. 12

[24] L.B. Dantas, H.R.B. Orlande, and R.M. Cotta. An inverse problem of parameter estimation for heat and mass transfer in capillary porous media. *International Journal of Heat and Mass Transfer*, 46(9):1587–1598, 2003. 13

[25] G.S. Dulikravich, T.J. Martin, B.H. Dennis, and N.F. Foster. *Multidisciplinary Hybrid Constrained GA Optimization, Invited lecture, Chapter 12 in EUROGEN'99 - Evolutionary Algorithms in Engineering and Computer Science: Recent Advances and Industrial Applications*. K. Miettinen, M. M. Makela, P. Neittaanmaki and J. Periaux, John Wiley Sons, Jyvaskyla, Finland, May 30-June 3, 1999. 13

[26] G.S. Dulikravich, T.J. Martin, M.J. Colaco, and J.E Inclan. Automatic switching algorithms in hybrid single-objective optimizers. *FME Transactions*, 41(3):167–179, 2013. 13

[27] K. Deb and H. Jain. An evolutionary many-objective optimization algorithm using reference-point-based nondominated sorting approach, part i: Solving problems with box constraints. *IEEE Transactions on Evolutionary Computation*, 18(4):577–601, 2014. 13

[28] T. Robic and B. Filipic. DEMO: Differential Evolution for Multi- Objective Optimization. *Proceedings of 3rd International Conference on Evolutionary Multi-Criterion Optimization, LNCS 3410*, 18(4):520–533, 2005. 13

[29] K. Li, K. Deb, Q. Zhang, and S. Kwong. An evolutionary many-objective optimization algorithm based on dominance and decomposition. *IEEE Transactions on Evolutionary Computation*, 19(5):694–716, 2015. 13

[30] T. Busser, M. Pailha, A. Piot, and M. Woloszyn. Simultaneous hygrothermal performance assessment of an air volume and surrounding highly hygroscopic walls. *Building and Environment*, 148:677–688, 2019. 13, 14

[31] J. R. Taylor. *An introduction to error analysis; the study of uncertainties in physical measurements*. University Science Books. 15

[32] E. Walter and Y. Lecourtier. Global approaches to identifiability testing for linear and nonlinear state space models. *Mathematics and Computers in Simulation*, 24(6):472–482, 1982. 16

[33] H. M. Kunzel and K. Kiessl. Calculation of heat and moisture transfer in exposed building components. *International Journal of Heat and Mass Transfer*, 40(1):159–167, 1996. 22

[34] O. Vololonirina, M. Coutand, and B. Perrin. Characterization of hygrothermal properties of wood-based products – impact of moisture content and temperature. *Construction and Building Materials*, 63:223–233, 2014. 22

[35] L. Wang and H. Ge. Hygrothermal performance of cross-laminated timber wall assemblies: A stochastic approach. *Building and Environment*, 97:11–25, 2016. 22